clones, according to the teratoma-forming activity of the iPS-derived neurospheres after transplantation into the NOD/SCID mouse brain.

Here, we first performed a detailed examination of the neural differentiation potential of a safe iPS clone, 38C2, which was established from mouse embryonic fibroblasts (MEFs) by the introduction of four factors, including *c-Myc*, and by the selection for *Nanog* expression (19, 28), and compared them with mouse ES cells (EB3) (29, 30). 38C2 iPS cells and EB3 ES cells were induced into embryoid bodies (EBs) in medium containing a low concentration of retinoic acid, then dissociated and cultured in suspension in serum-free medium with FGF-2 for 7 or 8 d to form primary neurospheres (PNS) (38C2 iPS/EB3 ES-PNS) (29). These PNSs were dissociated and formed secondary neurospheres (38C2 iPS/EB3 ES-SNS) under the same conditions (Fig. 1*A*). To induce further differentiation, 38C2 iPS-SNSs were adherently cultured in the absence of FGF-2, resulting in the generation of Tuj1$^+$ neurons (4.9 ± 0.8%), GFAP$^+$ astrocytes (11.3 ± 1.2%), and CNPase$^+$ oligodendrocytes (3.7 ± 0.9%), as well as Nestin$^+$ neural progenitor cells (25.9 ± 6.5%; Fig. 1 *B* and *C*), suggesting that 38C2 iPS-SNS have similar differentiation potentials to EB3 ES-SNS. The 38C2 iPS-PNSs could also generate TH$^+$ catecholaminergic, 5HT$^+$ serotonergic, and GAD67$^+$ GABAergic neurons (Fig. S1). RT-PCR analysis of the expression of cell-type-specific markers in the progeny of the 38C2 iPS cells showed drastic decrease of the expression of undifferentiated ES cell marker genes, such as *Nanog*, *Eras*, and *Oct3/4*, and the up-regulation of neural markers such as *Sox1*, *βIII-tubulin*, and *GFAP* during the neural differentiation of 38C2 iPS cells, similar to EB3 ES cells (Fig. 1*D*).

Moreover, electrophysiological analysis using whole-cell patch clamping in both the 38C2 iPS-PNS– and EB ES-PNS–derived neurons after 21–28 d of adherent differentiation showed tetrodotoxin (TTX; 1 μM)-sensitive repetitive action potentials in the current-clamp mode [38C2 iPS-PNS (n = 11 of 16) and EB3 ES-PNS (n = 5 of 7)] (Fig. S2*A*) and very rapid inward currents immediately followed by transient outward currents in voltage-clamp mode (Fig. S2*B* 1 and 2). Steady outward currents, similar to those mediated by delayed-rectifier K$^+$ channels, were also observed (Fig. S2 *B*1 and *D*). These findings suggest that 38C2 iPS-PNSs produced neuronal cells equipped with functional channels that could generate and modify action potentials (*SI Text*).

Safe MEF-iPS Cells Can Differentiate into Trilineage Neural Cells in the Injured Spinal Cord Without Tumorigenesis. Previously, we confirmed that SNSs from the safe 38C2 MEF-iPS cell clone survived and showed no teratoma-forming activity in the NOD/SCID mouse brain for 24 wk after transplantation (27) (Fig. S3). 38C2 iPS-SNSs that were transplanted into the intact spinal cord survived and differentiated into trilineage neural cells without any tumorigenesis (Fig. S4). Next, to evaluate their therapeutic effects in the mouse SCI model, we transplanted 38C2 iPS-SNSs into the contused spinal cord 9 d after injury and compared them with EB3 ES-SNSs, using adult fibroblasts and PBS as controls. We also made a comparison with 38C2 iPS-PNSs, because we recently confirmed that the transplantation of ES cell-derived SNSs, but not PNSs, provides therapeutic benefit after SCI (31). We transplanted 38C2 iPS-SNSs that had been prelabeled by lentivirus to express both CBR*luc* and mRFP (32, 33) into the lesion epicenter 9 d after the injury. Bioluminescence imaging (BLI) analysis (34), which detects luciferase photon signals only from living cells, revealed an approximate graft survival rate of 18% at 35 d after transplantation (Fig. 2*A*). We also histologically confirmed that the grafted cells survived and exhibited no apparent evidence of tumorigenesis (Fig. 2*B*), and that there were no Nanog$^+$ cells (Fig. S5), at least during our observation

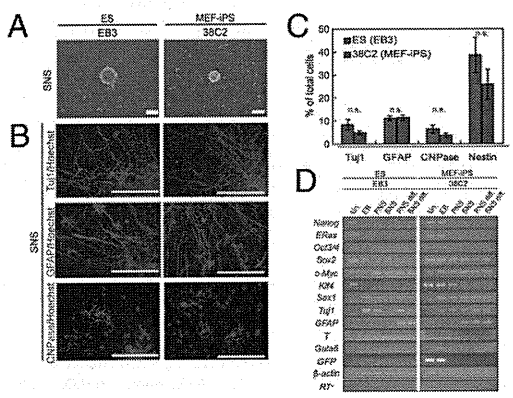

Fig. 1. Neural differentiation of pre-evaluated safe MEF-iPS cells in vitro. (*A*) Neurospheres derived from EB3 ES cells and 38C2 iPS cells. (Scale bar: 200 μm.) (*B*) Immunocytochemical analysis of neural cell marker proteins in the differentiated SNSs derived from EB3 ES and 38C2 iPS cells. (Scale bar: 100 μm.) (*C*) Neural differentiation efficiencies of neurospheres derived from EB3 ES and 38C2 iPS cells. (n = 5, n.s.). (*D*) RT-PCR analysis of undifferentiated cells (Un.), EBs, PNSs, SNSs, differentiated PNSs (PNS diff.), and SNSs (SNS diff.) of the EB3-ES and 38C2 iPS cells.

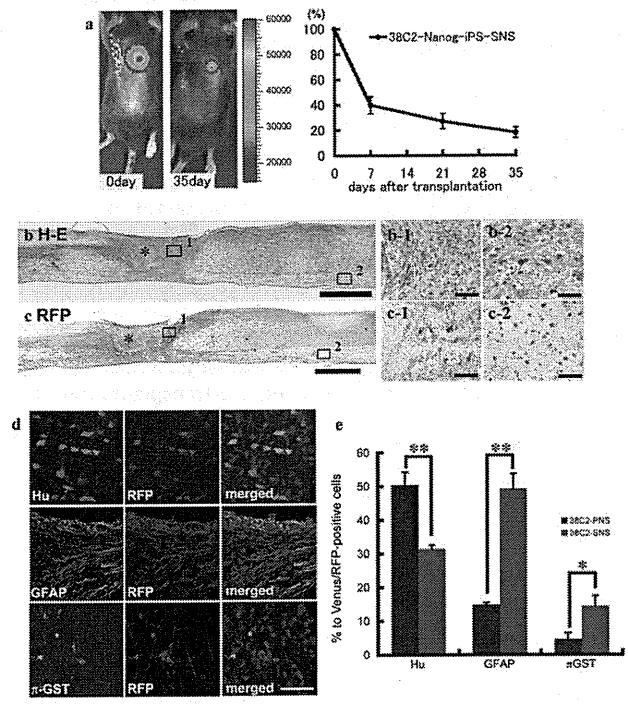

Fig. 2. Transplanted SNSs derived from safe MEF-iPS clones survive without any evidence of tumorigenesis and differentiate into trilineage neural cells in the injured spinal cord. (*A*) Representative BLI images of a mouse in which CBR*luc*-expressing 38C2 iPS-SNSs were transplanted into the injured spinal cord (*Left*, immediately after transplantation; *Right*, 42 d after transplantation). Quantification of the photon intensity revealed that ≈60% of the grafted cells were lost within 7 d after transplantation, and ≈20% of the cells survived 35 d after transplantation. Values are means ± SEM (n = 6). (*B*) H&E and (*C*) anti-RFP DAB staining of sagittal sections of the spinal cord 42 d after injury (38C2 iPS-SNS transplanted). There was no evidence of tumorigenesis (*B*). No significant nuclear atypia was observed in magnified images of the boxed areas showing the lesion epicenter (*B*-1) or white matter caudal to the transplantation site (*B*-2). Grafted cells survived and were diffusely distributed rostral and caudal to the lesion site (*C*). Higher-magnification images of the boxed areas showing the lesion site (C-1) and white matter caudal to the lesion site (C-2). *Lesion epicenter. (*D*) Immunohistochemical analyses of 38C2 iPS-SNSs grafted into spinal cord 42 d after injury, revealing grafted cells double-positive for RFP and markers of neural lineages. (*E*) Quantitative analyses of Hu$^+$ neurons, GFAP$^+$ astrocytes, and π-GST$^+$ oligodendrocytes. Values are means ± SEM (n = 3 each; *P < 0.05, **P < 0.01).

NEUROSCIENCE

period. Grafted RFP$^+$ cells were located mainly around the lesion epicenter, whereas some cells had migrated as far as 4 mm rostral and caudal to the graft site (Fig. 2*C*). In the injured spinal cord, the grafted 38C2 iPS-SNSs differentiated into three types of neural cells, including Hu$^+$ neurons (31.4 ± 1.1%), GFAP$^+$ astrocytes (49.3 ± 4.5%), and π-GST$^+$ oligodendrocytes (14.4 ± 3.0%), whereas 38C2 iPS-PNSs differentiated dominantly into neurons—that is, Hu$^+$ neurons (50.4 ± 3.8%), GFAP$^+$ astrocytes (14.9 ± 0.6%), and π-GST$^+$ oligodendrocytes (4.6 ± 1.8%) (Fig. 2 *D* and *E* and Fig. S6).

Transplantation of SNSs Derived from Safe MEF-iPS Cells into the Injured Spinal Cord Promotes Functional Recovery. The contusive SCI initially caused complete paralysis, followed by gradual recovery that reached a plateau. There were statistically significant differences in Basso mouse scale (BMS) between the 38C2 iPS-SNS and PBS groups at 21, 28, 35, and 42 d after injury, whereas no significant difference was observed between the 38C2 iPS-SNS and EB3 ES-SNS groups. Forty-two days after injury, the 38C2 iPS-SNS–grafted animals could lift their trunks and had significantly better BMS than the PBS control or adult fibroblast-treated animals, which were unable to support their body weight with their hindlimbs (Fig. 3*A*). To reveal the potential mechanism of functional recovery after 38C2 iPS-SNS transplantation, we conducted further histological analyses. By Luxol Fast Blue (LFB) staining, 38C2 iPS-SNS–grafted mice showed a significantly larger myelinated area at the lesion epicenter than the PBS control mice at 42 d after injury (Fig. 3*B*). We also found that grafted 38C2 iPS-SNS–derived cells myelinated NF200$^+$ host neuronal fibers, confirmed by the positive staining of RFP and myelin basic protein (MBP; Fig. 3*C*), indicating that graft cell-derived oligodendrocytes were capable of remyelination. For further confirmation of the myelinating ability of 38C2 iPS-SNSs, we transplanted 38C2 iPS-SNSs into the injured spinal cord of MBP-null *shiverer* mice, a severely hypo- and dysmyelinating mutant mouse that lacks the major dense line of CNS myelin (35). Myelinating potential of the grafted 38C2 iPS-SNS–derived cells was confirmed, exhibiting MBP$^+$ deposits (Fig. 3*D*) and the major dense line, by electron microscopic analysis (Fig. 3*E*).

To determine the effect of the grafted 38C2 iPS-SNSs on serotonergic nerve fibers, which are important for the motor functional recovery of hind limbs (36, 37), we immunostained for 5HT and quantified the positive area at the distal cord 1, 2, and 6 wk after injury. Some of the nerve fibers associated with graft cell-derived Hu$^+$ neurons were identified as 5HT$^+$ serotonergic fibers, and were prominent at the distal cord compared with the PBS control group (Fig. 4 *A–C*). Quantitative analysis of the serotonergic innervation of the distal cord revealed a significant difference between the 38C2 iPS-SNS and PBS control groups (Fig. 4*B*). The contusive injury (60 kDyn) resulted in a significant decrease in the number of 5HT$^+$ fibers at the distal cord, followed by a slight recovery, which is the nature of contusive SCI. The injection of PBS in the PBS control group did not induce any additional increase in the number of 5HT$^+$ fibers at the distal cord. In contrast, innervation of the distal cord by these 5HT$^+$ fibers was enhanced by the grafted 38C2 iPS-SNS 6 wk after SCI (Fig. 4*B*). Moreover, 38C2 iPS-SNS–derived astrocytes, which exhibited a bipolar morphology with long processes, were observed closely associated with the 5HT$^+$ serotonergic fibers (Fig. 4*D*).

Transplantation of Neurospheres Derived from Pre-Evaluated Safe or Unsafe TTF-iPS Cells into the Injured Spinal Cord. Toward the goal of clinical application, we next examined the therapeutic potential

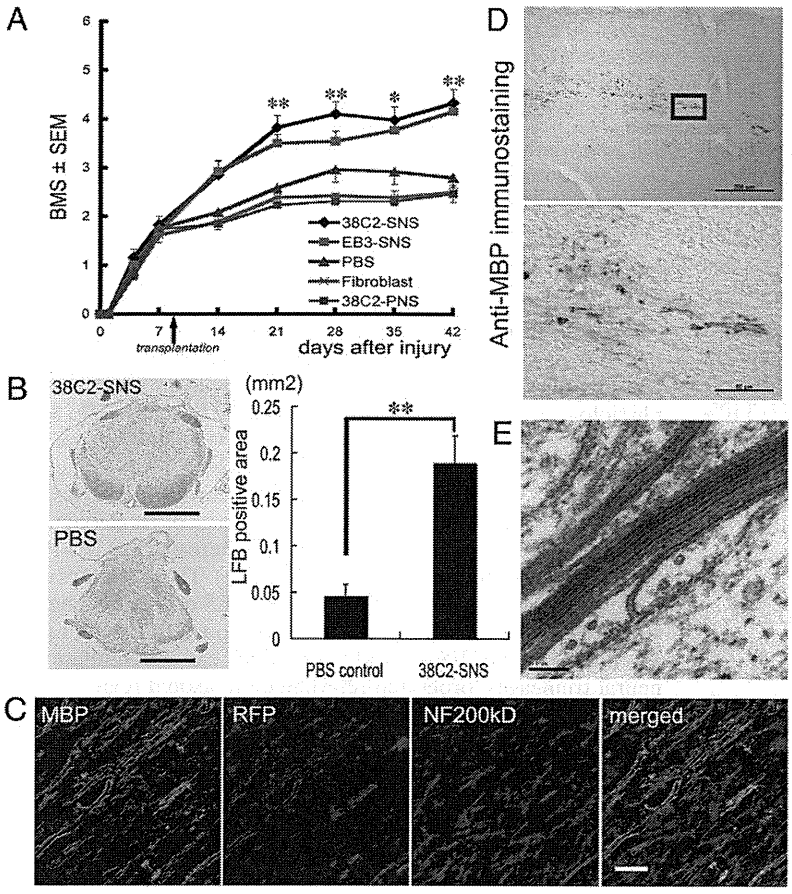

Fig. 3. SNS derived from a safe MEF-iPS clone differentiate into mature oligodendrocytes and promote remyelination. (*A*) Time course of functional recovery of hind limbs evaluated by BMS. 38C2 iPS-SNS, $n = 19$; EB3 ES-SNS, $n = 15$; PBS, $n = 12$; adult fibroblasts, $n = 13$; 38C2 iPS-PNS, $n = 13$. $^*P < 0.05$, $^{**}P < 0.01$. (*B*) LFB staining of axial sections of the spinal cord at the lesion epicenter 42 d after injury; 38C2 iPS-SNS–transplanted (*Upper Left*) and PBS control (*Lower Left*) animals. Quantification of LFB-positive areas at the lesion epicenter 42 d after injury (*Right*, $n = 7$ each; $^{**}P < 0.01$). (*C*) Immunohistochemistry of 38C2 iPS-SNS–derived mature oligodendrocytes (MBP$^+$). Grafted cells were integrated into myelin sheath. (*D*) Anti-MBP DAB staining of sagittally sectioned spinal cord of a *shiverer* mouse 8 wk after transplantation. MBP$^+$ myelin was detected in the area caudal to the lesion epicenter. (*Lower*) Higher-magnification image of the boxed area. (*E*) EM pictures of the injured spinal cord of a 38C2 iPS-SNS–grafted *shiverer* mouse exhibiting a prominent major dense line and intraperiod lines in multiple compacted lamellae. (Scale bars: *B*, 500 μm; *D Upper*, 200 μm; *C* and *D Lower*, 50 μm; and *E*, 0.1 μm.)

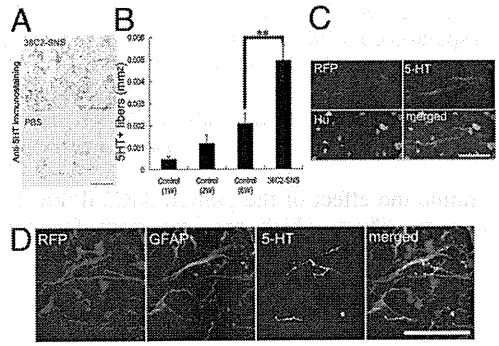

Fig. 4. SNSs derived from a safe MEF-iPS clone promote serotonergic innervation of the dorsal cord and result in better functional recovery of the hindlimbs. (*A*) 38C2 iPS-SNS transplantation promoted the growth of 5HT$^+$ serotonergic fibers in the distal spinal cord. Axial sections of 38C2 iPS-SNS–transplanted (*Upper*) and PBS control mice (*Lower*). (*B*) Quantitative analysis of 5HT$^+$ serotonergic fibers of distal cord in the PBS control (1, 2, and 6 wk postinjury) and 38C2 iPS-SNS transplantation groups (6 wk postinjury; 1 and 2 wk postinjury, $n = 3$ each; 6 wk postinjury and 38C2 SNS, $n = 7$ each; $^{**}P < 0.01$). (*C* and *D*) Immunohistochemistry of 38C2 iPS-SNS–derived neurons (*C*, RFP$^+$, Hu$^+$) and astrocytes (*D*, RFP$^+$, GFAP$^+$) closely associated with 5HT$^+$ serotonergic fibers. (Scale bars: *A*, 100 μm; *C*, 20 μm; *D*, 50 μm.)

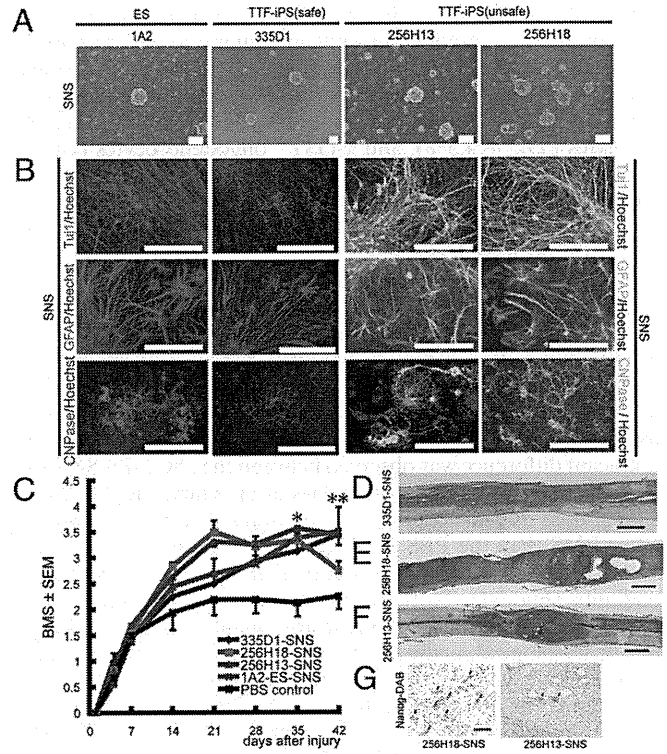

Fig. 5. Characterization and transplantation of SNSs derived from safe and unsafe TTF-iPS cells. (*A*) Neurospheres derived from 1A2 ES cells, 335D1, 256H13, and 256H18 iPS cells. (Scale bar: 200 μm.) (*B*) The differentiation potential of TTF-iPS-derived SNSs tested in vitro by immunocytochemical analyses of neural cell markers; Tuj1 for neurons, GFAP for astrocytes, and CNPase for oligodendrocytes. (Scale bar: 100 μm.) (*C*) Time course of functional recovery of the hindlimbs evaluated by BMS. 335D1 iPS-SNS: $n = 9$ each; 256H13 and 256H18 iPS-SNS: $n = 9$; 1A2 ES-SNS: $n = 9$; PBS control: $n = 8$. $^*P < 0.05$, $^{**}P < 0.01$. (*D–F*) H&E sagittal sections of the spinal cord 42 d after injury. (*D*) 335D1 iPS-SNS, (*E*) 256H18 iPS-SNS, and (*F*) 256H13 iPS-SNS grafted mice. There was no evidence of tumorigenesis in the 335D1 iPS-SNS grafted mice (*D*), whereas teratoma formation was detected within the injured spinal cord in both 256H18 iPS-SNS (*E*), and 256H13 iPS-SNS (*F*) grafted mice. (*G*) Anti-Nanog DAB staining of sagittally sectioned spinal cord of 256H18 and 256H13 iPS-SNS–transplanted animals 35 d after transplantation.

of adult tissue-derived iPS cells. Among six TTF-iPS clones pre-evaluated in our previous study (27), we used the safe 335D1 TTF-iPS clone, which was generated with *Nanog* selection and without the transduction of c-Myc. We also used the unsafe 256H13 and 256H18 TTF-iPS clones (22, 27), which were generated without genetic selection or the transduction of c-Myc, and were originally established from CAG-EGFP mice (22). A subclone of RF8 ES cells carrying the *Nanog*-EGFP reporter (1A2) (19) was used as control. All of the TTF-iPS clones formed PNSs and SNSs (Fig. 5*A*), and generated cells of all three neural lineages, similar to those derived from 1A2 ES cells (Fig. 5*B*). We transplanted these TTF-iPS–derived SNSs into injured spinal cords 9 d after injury. Transplantation of the safe 335D1 iPS-SNS (prelabeled with RFP lentivirally) resulted in better functional recovery compared with the PBS control group, without any apparent tumorigenesis during our observation period (Fig. 5 *C* and *D*). Grafted and survived RFP$^+$ 335D1 iPS-SNS–derived cells could differentiate into neural trilineages (Fig. S7 *A* and *B*). Furthermore, LFB staining revealed that 335D1 iPS-SNS–grafted mice had a significantly larger myelinated area at the lesion epicenter than the PBS control mice at 42 d after injury (Fig. S8 *A* and *B*), and grafted RFP$^+$ 335D1 SNS-derived cells differentiated into MBP$^+$ oligodendrocytes (Fig. S8*C*). However, all unsafe 256H18 iPS-SNS–grafted mice and one of 256H13 iPS-SNS–grafted mice formed teratomas containing EGFP$^+$ donor cells within the injured spinal cord (Fig. 5 *E* and *F* and Fig. S7*C*). Histological analyses revealed that these teratomas contained epithelial and smooth muscle tissue (Fig. S9*A*), and also exhibited Nanog immunoreactivity (Fig. 5*G*). Although the motor functions gradually recovered in both groups to the same extent as in the safe 335D1 iPS-SNS recipients until 35 d after injury, the 256H18 iPS-SNS–grafted animals exhibited a sudden deterioration of motor function 42 d after injury. In contrast, the 256H13 iPS-SNS–grafted animals maintained their functional recovery at 42 d after injury (Fig. 5*C*). Notably, in most mice of the 256H13 iPS-SNS group, scattered small clusters of Nanog$^+$ cells were observed in the spinal cords without obvious teratoma formation (Fig. S9 *B* and *C*). Thus, we speculate that teratoma formation and subsequent deterioration of function recovery would occur in the 256H13 group if a longer observation period was set.

Discussion

In the present study, we showed that the pre-evaluated safe iPS cells could produce neurospheres containing NS/PCs (Fig. 1*A*) that give rise to trilineage neural cells, including several types of neurons (Fig. 1 *B* and *C*), and that the neurons were electrophysiologically functional in vitro similar to ES cells (Fig. S2).

Based on these safety assessments and in vitro findings, we performed an in vivo study using the safe 38C2 MEF-iPS cell clone. Grafted 38C2 iPS-SNSs differentiated into neurons, astrocytes, and oligodendrocytes without forming teratomas or other tumors, and promoted functional recovery after SCI, whereas 38C2 iPS-PNSs did not show any therapeutic effects (Fig. 3*A*). These findings were compatible with our recent data on mouse ES cell-derived neurosphere transplantation into an identical mouse SCI model (31). Transplantation of ES-derived SNSs, which can differentiate into neural trilineages, promoted remyelination, axonal regrowth and tissue sparing, leading to improved function. In contrast, predominantly neurogenic PNSs showed no therapeutic effects on SCI (31). Thus, we elected to use iPS-SNSs and not iPS-PNSs for this study. In fact, the grafted 38C2 iPS-SNSs formed MBP$^+$ myelin sheaths within the injured spinal cord. We also confirmed the myelination potential of 38C2 iPS-SNS–derived cells in the spinal cord of the MBP-null *shiverer* mouse by electron microscopy (Fig. 3

D and *E*). These findings suggested the possibility of the remyelination of demyelinated axons by the grafted 38C2 iPS-SNS–derived oligodendrocytes, which may have contributed to the functional recovery of the grafted animals.

Another potential mechanism for functional recovery is axonal regrowth supported by iPS-SNS–derived astrocytes. Here, we observed grafted 38C2 iPS-SNS–derived $GFAP^+$ astrocytes, which exhibited a bipolar morphology with long processes extending along the axis of the spinal cord, caudal to the lesion epicenter, in close association with $5HT^+$ host serotonergic fibers (Fig. 4*D*). A previous report indicated that immature astrocytes derived from cells grafted into the injured spinal cord promote the outgrowth of $5HT^+$ fibers by offering a growth-permissive surface (38). Consistent with this finding, the transplantation of 38C2 iPS-SNSs promoted serotonergic innervation of the distal cord compared with the PBS control animals, thereby enhancing functional recovery after SCI (Fig. 4 *A* and *B*) (36). Furthermore, trophic factors, such as neurotrophin-3 (NT-3) and brain-derived neurotrophic factor (BDNF), were expressed in 38C2 iPS-SNSs, which could act as an integral part of the observed functional recovery (39, 40). The tissue sparing (e.g., neuroprotection, axon sprouting and remyelination) and other effects, including functional remodeling of spinal locomotor circuits (41), of trophic factors secreted from grafted cells are considered to be important for functional recovery (42). Thus, the combined effects of the 38C2 iPS-SNS–derived glial cells probably contributed to locomotor function recovery.

For clinical applications, the findings with TTF-iPS cells were promising, as most SCI patients are adults. The transplantation of SNSs derived from a pre-evaluated safe TTF-iPS clone promoted functional recovery after SCI without teratoma formation, like the SNSs from safe MEF-iPS clone did (Fig. 5*D*). However, the transplantation of SNSs derived from the unsafe TTF-iPS cells resulted in teratoma formation and functional deterioration. The teratoma-forming activity of TTF-iPS-SNSs could be caused by the presence of undifferentiated cells that might be resistant to differentiation signals within the SNSs (27). In fact, we recently reported that persistent presence of undifferentiated cells within iPS-SNSs highly correlated with teratoma-forming propensity, assayed by flow cytometric analysis using *Nanog*-EGFP reporter and transplantation into the brains of immunodeficient (NOD/SCID) (27). Before iPS cells of adult origin can be used clinically, important hurdles must still be overcome. Though new methods for establishing iPS cells are constantly being developed, including virus-free (43) and transgene-free (44) systems, a new strategy is needed to exclude undifferentiated cells from the differentiated progeny of iPS cells. These findings show that the pre-evaluation of iPS cells' in vitro differentiation potential could play a critical role in terms of their safety and therapeutic effects on the mouse SCI model. Thus, iPS-derived neurosphere transplantation has potential therapeutic use in SCI, when the iPS cell clones are carefully pre-evaluated.

From a clinical viewpoint, it is particularly encouraging that delaying the iPS-derived NS/PC transplantation (to 9 d after injury) enhanced both the survival of the grafted cells and functional recovery, the therapeutic effects of which is almost comparable to those of fetal CNS-derived NS/PCs transplantation (refs. 34 and 45). This finding may also be applicable to the treatment of patients with SCI. Since our first report of iPS cells (18), there has been increasing interest in their characteristics and therapeutic potential. Our present study demonstrates the therapeutic potential of iPS-derived NS/PCs for SCI repair. Before any clinical trial of human CNS disorders using iPS cells, it will be essential to pre-evaluate each iPS cell clone carefully to guarantee a safety level equal to other types of cells, such as Schwann cells (46, 47) and fetal-derived neurosphere cells (NS/PCs) (3), and to conduct preclinical transplantation studies using appropriate primate models (48, 49).

Methods

Reverse-Transcription and RT-PCR. RNA was isolated with TRIzol (Invitrogen) according to the manufacturer's instructions. Total RNA (0.5 μg) was treated with TURBO DNase (Ambion) and then reverse-transcribed with oligo (dT) primer and SuperScript III (Invitrogen). The primers and PCR conditions used in this study are listed Table S1.

Cell Culture, Neural Induction, and Immunocytochemistry. Mouse ES and iPS cells were cultured as described previously (19, 28, 29). Mouse ES and iPS cells were differentiated into neurospheres via EBs treated with 10^{-8} M retinoic acid (Sigma), as described previously with minor modification (28, 29). (Detailed differentiation protocol is described in *SI Text*.) ES and iPS cell-derived neurospheres were dissociated and differentiated on poly-L-ornithine/fibronectin-coated coverslips for 5 d and subjected to immunocytochemical analysis. The number of cells immunoreactive for each marker was counted and shown as the percentage of the total number of cells counterstained with Hoechst 33258. The antibodies used in this study are listed in Table S2.

Lentivirus Production and Infection of Secondary Neurospheres. For BLI tracing of grafted 38C2 iPS-SNSs, we generated a modified lentivirus vector encoding both the click beetle red luciferase (CBR*luc*; Promega) and mRFP, pCSII-EF-CBR*luc*-IRES2-mRFP (32, 33). For lentivirus preparation, HEK-293T cells were transfected with pCSII-EF-CBR*luc*-IRES2-mRFP, pCAG-HIVgp, and pCMV-VSV-G-RSV-Rev, and the conditioned medium containing virus particles was concentrated and used for viral transduction.

Spinal Cord Injury Model and Transplantation. Adult female C57BL/6J mice (20–22 g) were anesthetized via an i.p. injection of ketamine (100 mg/kg) and xylazine (10 mg/kg). A contusive spinal cord injury using an Infinite Horizon Impactor (60 kdyn; Precision Systems) was induced at the Th10 level as reported previously (34). For transplantation, 5×10^5 cells of mouse ES/iPS cell-derived neurospheres, adult dermal fibroblasts in 2 μL of cell suspension, or PBS was injected into the lesion epicenter. Hindlimb motor function was evaluated by the locomotor rating of the Basso mouse scale (BMS) (50) for 42 d after injury. For the in vivo imaging of intact and injured spinal cords after the transplantation, a Xenogen-IVIS 100 cooled CCD optical macroscopic imaging system (SC BioScience) was used for BLI, as reported previously (34) (*SI Text*). All procedures were approved by the ethics committee of Keio University, and were in accordance with the Guide for the Care and Use of Laboratory Animals (National Institutes of Health). Grafted animals were deeply anesthetized and intracardially perfused with 4% paraformaldehyde (PFA; pH 7.4). The dissected spinal cords were sectioned into 20-μm axial/sagittal sections using a cryostat and processed for histological analyses. Detailed conditions for histological analyses are described in *SI Text*.

Statistical Analysis. All data are reported as the mean ± SEM. An unpaired two-tailed Student's *t* test was used for the analyses of in vitro and in vivo 38C2 iPS-SNS and ES-SNS differentiation efficiency (Figs. 1*C* and 2*E*), $5HT^+$ areas (Fig. 4*B*), and LFB^+ areas (Fig. 2*B*). Repeated-measures two-way ANOVA, followed by the Tukey–Kramer test, was used for BMS analysis. $*P < 0.05$, $**P < 0.01$.

ACKNOWLEDGMENTS. We thank Drs. H. Abe, T. Sunabori, F. Renault-Mihara, W. Akamatsu, S. Shibata, T. Harada, S. Miyao, and H. J. Okano (Keio University) for technical assistance and scientific discussions, and all the members of Dr. Okano's and Dr. Yamanaka's laboratories for encouragement and generous support. We also thank Drs. K. Okita, M. Koyanagi, and K. Tanabe (Kyoto University) for the undifferentiated iPS cells, Dr. H. Niwa (Riken CDB) for the EB3 ES cells, Dr. R. Farese (University of California-San Francisco) for the RF8 ES cells, Dr. R. Y. Tsien (University of California-San Diego) for the mRFP gene, Dr. A. Miyawaki (Riken BSI) for the Venus gene, Dr. H. Baba (Tokyo University of Phamacy and Life Science) for the shiverer mice, and Dr. H. Miyoshi (Riken BRC) for the lentiviral vectors. We especially thank Drs. S. Okada (Kyusyu University), A. Iwanami (University of California-San Francisco and Keio University), and J. Yamane (Keio University) for scientific discussions, technical advice, and encouragement. This work was supported by grants from the Program for Promotion of Fundamental Studies in Health Sciences of the National Institute of Biomedical Innovation (NIBIO), a grant from Uehara Memorial Foundation, and Grants-in-Aid for Scientific Research from the Japan Society for the Promotion of Science (JSPS) and the Ministry of Education, Culture, Sports, Science and Technology of Japan (MEXT), the project for realization of regenerative medicine and support for the core institutes for iPS cell research from MEXT; Japan Science and Technology Agency (SORST); the Ministry of Health, Labor, and Welfare; the General Insurance Association of Japan; Research Fellowships for Young Scientists from the Japan Society for the Promotion of Science; Keio Gijuku Academic Development Funds; and a Grant-in-aid for the Global COE program from MEXT to Keio University.

1. Björklund A, Lindvall O (2000) Cell replacement therapies for central nervous system disorders. *Nat Neurosci* 3:537–544.
2. Okano H (2002) Stem cell biology of the central nervous system. *J Neurosci Res* 69: 698–707.
3. Lindvall O, Kokaia Z, Martinez-Serrano A (2004) Stem cell therapy for human neurodegenerative disorders—how to make it work. *Nat Med* 10 (Suppl):S42–S50.
4. Martino G, Pluchino S (2006) The therapeutic potential of neural stem cells. *Nat Rev Neurosci* 7:395–406.
5. Lindvall O, Kokaia Z (2006) Stem cells for the treatment of neurological disorders. *Nature* 441:1094–1096.
6. Gage FH (2000) Mammalian neural stem cells. *Science* 287:1433–1438.
7. Wichterle H, Lieberam I, Porter JA, Jessell TM (2002) Directed differentiation of embryonic stem cells into motor neurons. *Cell* 110:385–397.
8. Watanabe K, et al. (2005) Directed differentiation of telencephalic precursors from embryonic stem cells. *Nat Neurosci* 8:288–296.
9. Sonntag KC, et al. (2007) Enhanced yield of neuroepithelial precursors and midbrain-like dopaminergic neurons from human embryonic stem cells using the bone morphogenic protein antagonist noggin. *Stem Cells* 25:411–418.
10. Tropepe V, et al. (2001) Direct neural fate specification from embryonic stem cells: A primitive mammalian neural stem cell stage acquired through a default mechanism. *Neuron* 30:65–78.
11. Ying QL, Stavridis M, Griffiths D, Li M, Smith A (2003) Conversion of embryonic stem cells into neuroectodermal precursors in adherent monoculture. *Nat Biotechnol* 21: 183–186.
12. McDonald JW, et al. (1999) Transplanted embryonic stem cells survive, differentiate and promote recovery in injured rat spinal cord. *Nat Med* 5:1410–1412.
13. Brüstle O, et al. (1999) Embryonic stem cell-derived glial precursors: A source of myelinating transplants. *Science* 285:754–756.
14. Kim JH, et al. (2002) Dopamine neurons derived from embryonic stem cells function in an animal model of Parkinson's disease. *Nature* 418:50–56.
15. Sharp J, Keirstead HS (2007) Therapeutic applications of oligodendrocyte precursors derived from human embryonic stem cells. *Curr Opin Biotechnol* 18:434–440.
16. Keirstead HS, et al. (2005) Human embryonic stem cell-derived oligodendrocyte progenitor cell transplants remyelinate and restore locomotion after spinal cord injury. *J Neurosci* 25:4694–4705.
17. Hochedlinger K, Jaenisch R (2006) Nuclear reprogramming and pluripotency. *Nature* 441:1061–1067.
18. Takahashi K, Yamanaka S (2006) Induction of pluripotent stem cells from mouse embryonic and adult fibroblast cultures by defined factors. *Cell* 126:663–676.
19. Okita K, Ichisaka T, Yamanaka S (2007) Generation of germline-competent induced pluripotent stem cells. *Nature* 448:313–317.
20. Wernig M, et al. (2007) In vitro reprogramming of fibroblasts into a pluripotent ES-cell-like state. *Nature* 448:318–324.
21. Maherali N, et al. (2007) Directly reprogrammed fibroblasts show global epigenetic remodeling and widespread tissue contribution. *Cell Stem Cell* 1:55–70.
22. Nakagawa M, et al. (2008) Generation of induced pluripotent stem cells without Myc from mouse and human fibroblasts. *Nat Biotechnol* 26:101–106.
23. Wernig M, Meissner A, Cassady JP, Jaenisch R (2008) c-Myc is dispensable for direct reprogramming of mouse fibroblasts. *Cell Stem Cell* 2:10–12.
24. Hanna J, et al. (2007) Treatment of sickle cell anemia mouse model with iPS cells generated from autologous skin. *Science* 318:1920–1923.
25. Wernig M, et al. (2008) Neurons derived from reprogrammed fibroblasts functionally integrate into the fetal brain and improve symptoms of rats with Parkinson's disease. *Proc Natl Acad Sci USA* 105:5856–5861.
26. Yamanaka S (2007) Strategies and new developments in the generation of patient-specific pluripotent stem cells. *Cell Stem Cell* 1:39–49.
27. Miura K, et al. (2009) Variation in the safety of induced pluripotent stem cell lines. *Nat Biotechnol* 27:743–745.
28. Okada Y, et al. (2008) Spatiotemporal recapitulation of central nervous system development by murine embryonic stem cell-derived neural stem/progenitor cells. *Stem Cells* 26:3086–3098.
29. Okada Y, Shimazaki T, Sobue G, Okano H (2004) Retinoic-acid-concentration-dependent acquisition of neural cell identity during in vitro differentiation of mouse embryonic stem cells. *Dev Biol* 275:124–142.
30. Niwa H, Miyazaki J, Smith AG (2000) Quantitative expression of Oct-3/4 defines differentiation, dedifferentiation or self-renewal of ES cells. *Nat Genet* 24:372–376.
31. Kumagai G, et al. (2009) Roles of ES cell-derived gliogenic neural stem/progenitor cells in functional recovery after spinal cord injury. *PLoS ONE* 4:e7706.
32. Masuda H, et al. (2007) Noninvasive and real-time assessment of reconstructed functional human endometrium in NOD/SCID/gamma c(null) immunodeficient mice. *Proc Natl Acad Sci USA* 104:1925–1930.
33. Miyoshi H, Blömer U, Takahashi M, Gage FH, Verma IM (1998) Development of a self-inactivating lentivirus vector. *J Virol* 72:8150–8157.
34. Okada S, et al. (2005) In vivo imaging of engrafted neural stem cells: Its application in evaluating the optimal timing of transplantation for spinal cord injury. *FASEB J* 19: 1839–1841.
35. Inoue Y, et al. (1986) Alteration of the primary pattern of central myelin in a chimaeric environment—study of shiverer ↔ wild-type chimaeras. *Brain Res* 391:239–247.
36. Bregman BS, et al. (1993) Recovery of function after spinal cord injury: Mechanisms underlying transplant-mediated recovery of function differ after spinal cord injury in newborn and adult rats. *Exp Neurol* 123:3–16.
37. Nygren LG, Fuxe K, Jonsson G, Olson L (1974) Functional regeneration of 5-hydroxytryptamine nerve terminals in the rat spinal cord following 5, 6-dihydroxytryptamine induced degeneration. *Brain Res* 78:377–394.
38. Hofstetter CP, et al. (2002) Marrow stromal cells form guiding strands in the injured spinal cord and promote recovery. *Proc Natl Acad Sci USA* 99:2199–2204.
39. Widenfalk J, Lundströmer K, Jubran M, Brene S, Olson L (2001) Neurotrophic factors and receptors in the immature and adult spinal cord after mechanical injury or kainic acid. *J Neurosci* 21:3457–3475.
40. McTigue DM, Horner PJ, Stokes BT, Gage FH (1998) Neurotrophin-3 and brain-derived neurotrophic factor induce oligodendrocyte proliferation and myelination of regenerating axons in the contused adult rat spinal cord. *J Neurosci* 18:5354–5365.
41. Courtine G, et al. (2009) Transformation of nonfunctional spinal circuits into functional states after the loss of brain input. *Nat Neurosci* 12:1333–1342.
42. Lu P, Tuszynski MH (2008) Growth factors and combinatorial therapies for CNS regeneration. *Exp Neurol* 209:313–320.
43. Okita K, Nakagawa M, Hyenjong H, Ichisaka T, Yamanaka S (2008) Generation of mouse induced pluripotent stem cells without viral vectors. *Science* 322:949–953.
44. Zhou H, et al. (2009) Generation of induced pluripotent stem cells using recombinant proteins. *Cell Stem Cell* 4:381–384.
45. Ogawa Y, et al. (2002) Transplantation of in vitro-expanded fetal neural progenitor cells results in neurogenesis and functional recovery after spinal cord contusion injury in adult rats. *J Neurosci Res* 69:925–933.
46. Pearse DD, et al. (2004) cAMP and Schwann cells promote axonal growth and functional recovery after spinal cord injury. *Nat Med* 10:610–616.
47. Pearse DD, et al. (2007) Transplantation of Schwann cells and/or olfactory ensheathing glia into the contused spinal cord: Survival, migration, axon association, and functional recovery. *Glia* 55:976–1000.
48. Iwanami A, et al. (2005) Establishment of graded spinal cord injury model in a nonhuman primate: The common marmoset. *J Neurosci Res* 80:172–181.
49. Iwanami A, et al. (2005) Transplantation of human neural stem cells for spinal cord injury in primates. *J Neurosci Res* 80:182–190.
50. Basso DM, et al. (2006) Basso Mouse Scale for locomotion detects differences in recovery after spinal cord injury in five common mouse strains. *J Neurotrauma* 23:635–659.

Hindawi Publishing Corporation
Journal of Biomedicine and Biotechnology
Volume 2011, Article ID 157458, 7 pages
doi:10.1155/2011/157458

Research Article

Novel Concept of Motor Functional Analysis for Spinal Cord Injury in Adult Mice

Munehisa Shinozaki,[1,2] Yuichiro Takahashi,[3] Masahiko Mukaino,[4] Nobuhito Saito,[2] Yoshiaki Toyama,[3] Hideyuki Okano,[1] and Masaya Nakamura[3]

[1] *Department of Physiology, Keio University School of Medicine, Shinjuku, Tokyo 160-8582, Japan*
[2] *Department of Neurosurgery, Graduate School of Medicine, University of Tokyo, Tokyo 113-8655, Japan*
[3] *Department of Orthopedic Surgery, Keio University School of Medicine, Shinjuku, Tokyo 160-8582, Japan*
[4] *Department of Rehabilitation Medicine, Keio University School of Medicine, Shinjuku, Tokyo 160-8582, Japan*

Correspondence should be addressed to Masaya Nakamura, masa@sc.itc.keio.ac.jp

Received 9 September 2010; Accepted 2 December 2010

Academic Editor: Monica Fedele

In basic research on spinal cord injury (SCI), behavioral evaluation of the SCI animal model is critical. However, it is difficult to accurately evaluate function in the mouse SCI model due to the small size of mice. Although the open-field scoring scale is an outstanding appraisal method, supplementary objective tests are required. Using a compact SCANET system, in which a mouse carries out free movement for 5 min, we developed a novel method to detect locomotor ability. A SCANET system samples the horizontal coordinates of a mouse every 0.1 s, and both the speed and acceleration of its motion are calculated at each moment. It was found that the maximum speed and acceleration of motion over 5 min varied by injury severity. Moreover, these values were significantly correlated with open-field scores. The maximum speed and acceleration of SCI model mice using a SCANET system are objective, easy to obtain, and reproducible for evaluating locomotive function.

1. Introduction

In basic research on spinal cord injury (SCI), accurate evaluation of motor function in animal models is important. Although the Basso-Beattie-Bresnahan (BBB) score and the Basso Mouse Scale (BMS) are widely used [1, 2], objective supplemental tests are desirable, and various methods have been developed [3–8]. However, with any method of observing the motion of an animal, detection of the best performance of the hindlimbs is almost impossible, since the animal does not perform as the observer intends. A novel method to evaluate the maximum locomotor ability of a mouse using the SCANET system is presented [9]. SCANET system is originally a device which measures voluntary motor activity of an animal. It consists of 45-cm-square Plexiglas cage, frames which contain infrared sensors and enclose the cage, and a notebook computer. Infrared sensors were horizontally placed throughout the cage, and the *X*-*Y* coordinates of a freely moving animal in the box were recorded every 0.1 s. After recording for 5 min, the change in the coordinates per unit time was calculated for the speed, and the change in the speed per unit time was calculated as the acceleration. The maximum speed and maximum acceleration extracted from the 5 min of data were taken as the best locomotor function. There were significant differences in these parameters among the contusion, the transection, and the control groups throughout the observation period, and, especially in the contusion group, they were significantly correlated with the BMS score during the recovery process.

2. Materials and Methods

2.1. Spinal Cord Injury Model. Seventeen 6-week-old adult female C57BL/6J mice were used. The mice were anesthetized with an intraperitoneal injection of ketamine (100 mg/kg) and xylazine (10 mg/kg). The dorsal surface of the dura mater at the T10 level was exposed by laminectomy, and spinal cord injury was induced by (1) producing moderate

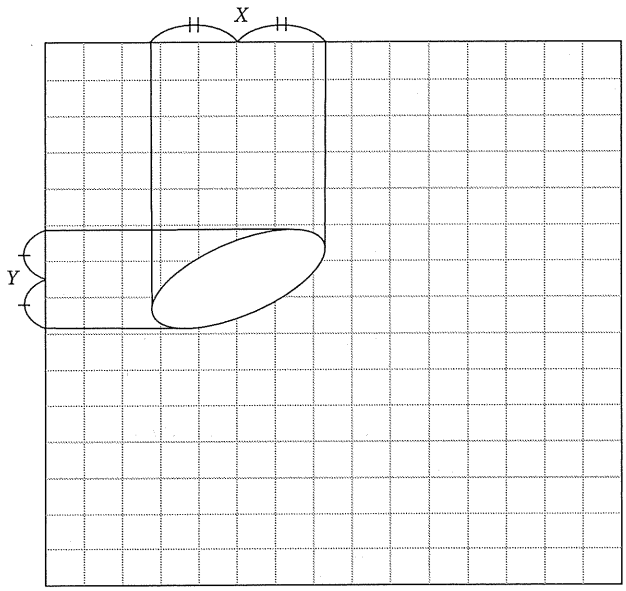

FIGURE 1: Schema of the inside of the Plexiglas cage. An ellipse expressed a mouse. Infrared sensors were arranged in a grid pattern, and the coordinates X and Y of the center of the object were recorded continuously.

contusion with an IH impactor ($n = 6$, impact force = 60 kdyn), as reported previously [10] or (2) transecting the spinal cord transversely with microscissors ($n = 6$). Only laminectomy was performed in the control group ($n = 5$). The muscles and skin were closed in layers, and the animals were placed in a temperature-controlled chamber until thermoregulation was re-established. Manual voiding of the bladder was performed twice per day until reflex bladder emptying was re-established. All the experiments and procedures in our study were approved by the Keio University Animal Research Committee in accordance with the Laboratory Animal Welfare Act, the Guide for the Care and Use of Laboratory Animals (National Institutes of Health, Bethesda, USA), and the Guidelines and Policies for Animal Surgery provided by the Animal Study Committees of the Central Institute for Experimental Animals and of Keio University.

2.2. Basso Mouse Scale Score. Motor function of the hindlimbs was evaluated by open-field testing using the methodology of the Basso Mouse Scale (BMS) score on postoperative days (POD) 1, 7, 14, 21, 28, 35, and 42, as described by Basso et al. [2].

2.3. SCANET. The SCANET MV-40 (MELQUEST Co., Ltd., Toyama, Japan) is an automatic analysis system for measuring the locomotor activity of small animals that has been previously described in [9, 11]. Briefly, infrared sensors are arranged in a horizontal plane of a transparent Plexiglas box of 45 cm around to make a sensor field with a 6-mm grid pattern. When something interferes with the paths of the infrared rays, the coordinates of the center of the object

TABLE 1: An example of the list of raw data, calculated speed, and acceleration.

Time (mm:ss.f)	X	Y	Speed (m/s)	Acceleration (m/s^2)
—	—	—	—	—
—	$X1$	$Y1$	—	—
—	$X2$	$Y2$	$S1$	—
59:09.6	3.5	8.5	$S2$	$A1$
59:09.7	4.0	9.0	0.0424	$A2$
59:09.8	4.0	7.0	0.1200	0.7757
59:09.9	5.0	5.5	0.1082	−0.1183
59:10.0	6.5	4.5	0.1082	0.0000
59:10.1	6.0	7.0	0.1530	0.4480
59:10.2	4.0	16.0	0.5532	4.0020
—	—	—	—	—

are recorded in a computer every 0.1 s (Figure 1). Moreover, by inserting another sensor frame perpendicularly, we can simultaneously observe at different height levels and detect rearing of the mouse. The height of the lower frame was set at 1.5 cm from the floor, and the upper frame was 9.5 cm from the floor. We waited for 10 s after putting each mouse into the box until it calmed down, and then we measured for 5 min. The test was conducted 1, 7, 14, 21, 35, and 42 days after injury in the same environment. The default data obtained by SCANET system are "M1," which is the number of episodes of movement longer than 12 mm "M2," which is the number of episodes of movement longer than 60 mm; "RG," which is the number of episodes of rearing. However, the X and Y coordinates are recorded as raw data every 0.1 s and are available from the computer (Table 1). From these, the amount of the distance moved per unit time (speed) and the change in the speed per unit time (acceleration) were calculated at each instant of time. Since the time interval was 0.1 s and the unit length in raw data was 0.6 cm, speed and acceleration were calculated as follows:

$$\text{Speed } (S1) = \left\{(X2 \times 0.006 - X1 \times 0.006)^2 + (Y2 \times 0.006 - Y1 \times 0.006)^2\right\}^{0.5} \times 10\,(\text{m/s}), \quad (1)$$

$$\text{Acceleration } (A1) = (S2 - S1) \times 10\,(\text{m/s}^2).$$

Then, the maximum speed and the maximum acceleration were extracted from the whole 5 min of data as measures of the best locomotor function. Since the SCANET system sometimes lacks the time or coordinate data for a moment, only successive data were used.

2.4. Histological Analysis. To confirm the reproducibility of SCI model in each mouse, histological analysis was performed. 56 days after SCI, all animals were deeply anesthetized with an intraperitoneal injection of ketamine (100 mg/kg) and xylazine (10 mg/kg) and transcardially perfused with 4% paraformaldehyde in 0.1 M phosphate-buffered saline (PBS). The spinal cord tissue was removed

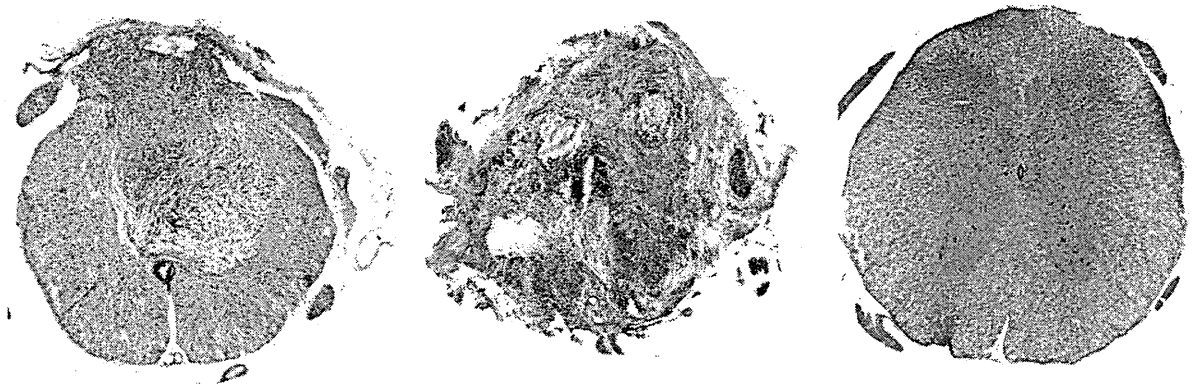

(a) (b) (c)

FIGURE 2: HE staining of representative axial spinal cord sections from the three groups of mice. (a) Contusion model: the ventral part of the spinal cord tissue was preserved, whereas the dorsal part was replaced by fibrous scar tissue after SCI. (b) Transection model: normal structure of the spinal cord totally disappeared. (c) Control mouse.

and postfixed in 4% paraformaldehyde in PBS for a few hours at room temperature. The tissue samples were immersed in 10% sucrose in PBS at 4°C for 24 hs, placed in 30% sucrose in PBS for 48 hs, and embedded in OTC compound. The embedded tissue was immediately frozen in liquid nitrogen and stored at −80°C until use. Frozen spinal cord tissues were sectioned on a cryostat at 20 μm in the axial plane. The sections were dried and stained with hematoxylin and eosin.

2.5. Statistics Analysis. All values are reported as the means ± SEM. Between-group comparisons were made by analysis of variance (ANOVA) followed by Scheffe's post hoc test at each postinjury time point. The strength of correlation with the BMS score was determined using the Pearson correlation coefficient.

3. Result

3.1. Histological Findings. The representative axial sections of the transection and contusion groups are shown in Figure 2. In the contusion group, infiltration of the inflammatory cells was observed at the dorsal part of the lesion site, and the ventral part of the spinal cord was preserved (Figure 2(a)). On the other hand, in the transection group, normal construction of the spinal cord was totally destroyed and replaced by inflammatory cells and fibrous tissues (Figure 2(b)).

3.2. BMS Score. Both the contusion and the transection injury resulted in complete paraplegia on POD 1 (Figure 3(a)). Although the BMS scores of the transection group did not show any recovery, those of the contusion group gradually increased and reached a plateau around a score of 4 on POD 14. Significant differences in BMS scores were observed among the three groups at all time points examined, except for POD 1.

3.3. Evaluation by SCANET. The control group showed the highest values of M1, M2, speed, and acceleration, followed by the contusion group and the transection group (Figure 3). The contusion and transection groups had very low RG numbers, while the control group had a stable number of RGs (Figure 3(d)). There were no significant differences in M1 and M2 among the three groups, except on PODs 1 and 21 (Figure 3(b)). However, speed was significantly different on PODs 14, 35, and 42 among the three groups, and the acceleration was significantly different on PODs 35 and 42 (Figures 3(e) and 3(f)). These results suggest that speed and acceleration reflected the severity of spinal cord injury better than M1 and M2 in the chronic phase of SCI.

3.4. Correlation between BMS Score and Speed/Acceleration of Movement. The correlation diagrams of M1, M2, speed, and acceleration with the BMS score in the contusion group are shown in Figure 4. Since M1 and M2 decreased gradually despite the increase in BMS score, there were no significant correlations between the BMS score and M1 and M2. On the other hand, speed and acceleration increased gradually, and the speed showed a significant correlation with the BMS score. These results suggest that the speed and acceleration are the best measures for observing functional recovery, not only to reflect the severity of injury.

3.5. Specific Features of Speed and Acceleration. For the BMS score, 5 min of observation are required for each mouse, so the same observation period was adopted for the present method. In order to examine how many minutes were suitable for the evaluation of the animal's performance by SCANET, the maximum speed of the mice on POD 42 was plotted for each time-duration (Figure 5). The maximum speed gradually increased and reached a plateau within 2 min in all groups. Therefore, 5 min were sufficient, and an even shorter examination time might has been enough for the SCANET evaluation.

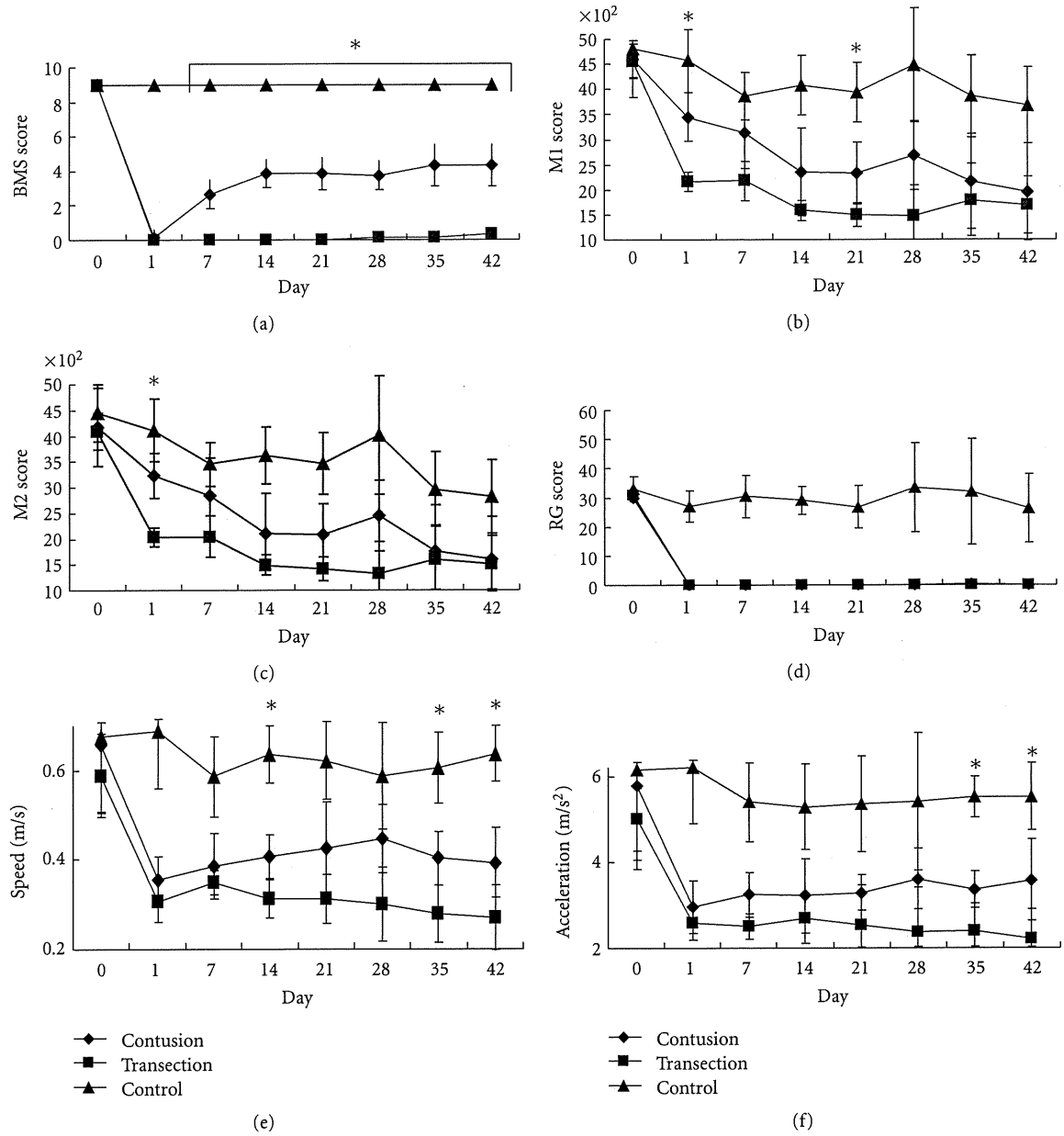

FIGURE 3: Time course of each parameter. (a) BMS score. (b) M1 score. (c) M2 score. (d) Rearing score (RG). (e) Speed. (f) Acceleration. M1 and M2 scores hardly showed a difference between the contusion and transection groups after 1 week, and they gradually decreased despite the animal's recovery of BMS score. The speed and acceleration showed clear differences among the three groups, especially in the late phase of SCI. $^*P < .05$.

The changes in speed and acceleration just before the maximum speed were also investigated, because we hypothesized that the mice with high BMS reached the maximum speed in a moment with their high instantaneous force, while the mice with low BMS increased their speed gradually. All mice reached the top speed within 0.1 s from a certain speed (Figure 6). The acceleration tended to decrease just before the maximum speed, and this might reflect the "premotion silent period" (exhaustion just before putting power into a voluntary muscle [12]) of an animal, because acceleration and muscle power were strongly correlated by the equation Force = Mass × Acceleration.

4. Discussion

In the present study, measurements of the maximum speed and acceleration of SCI model mice were found to be good indicators of the mice's motor performance, because they were constant in the control and transection groups and increased in the contusion group during the recovery of hindlimb function. In the transection group, the mice were not able to move their hindlimbs at all, but performed at half the speed of the control mice with only their forelimbs.

In this system, the moment of the best performance of a freely moving mouse can be detected. Therefore,

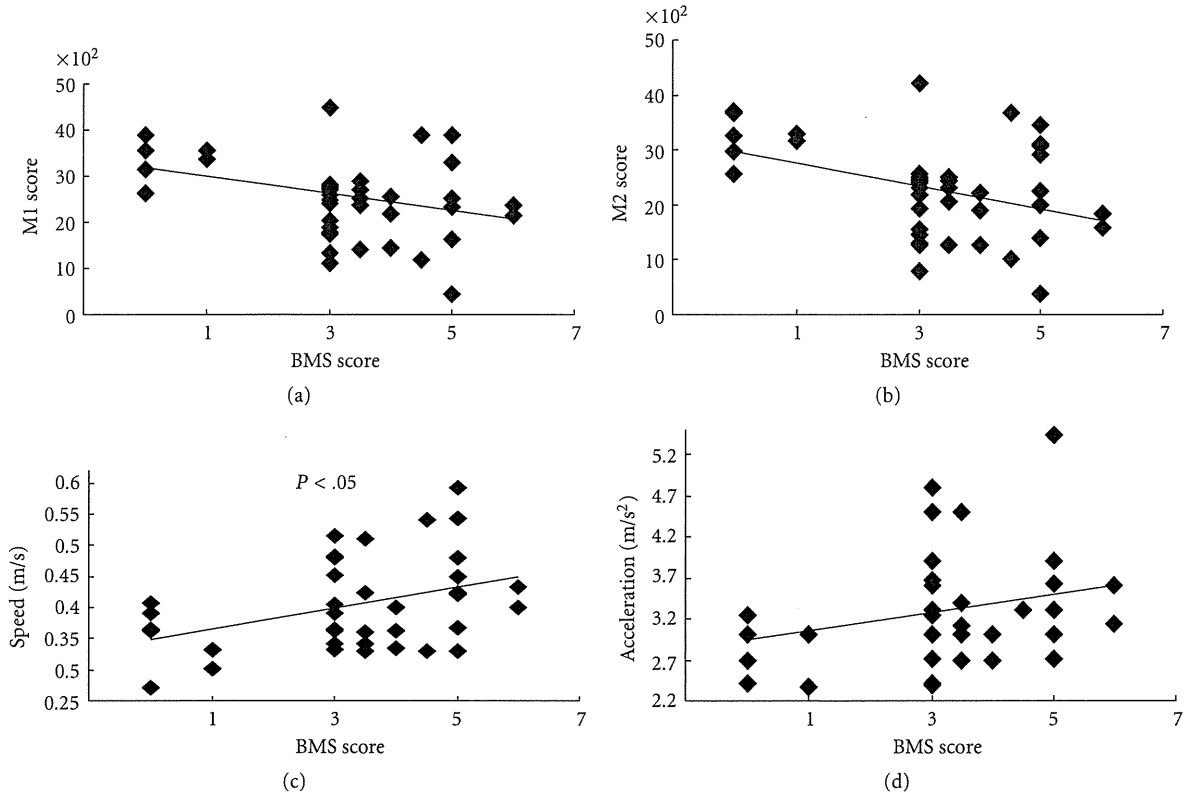

FIGURE 4: Correlation diagrams of parameters. M1 and M2 scores had minus correlations with the BMS score, while the speed and acceleration showed a strong correlation. Coefficients of correlation are −0.84 for M1 and BMS, −0.83 for M2 and BMS, 0.75 for speed and BMS, and 0.77 for acceleration and BMS.

the speed and acceleration may increase unwillingly if a mouse jumps by being surprised at a noise or a mouse is upset just after being put in the SCANET box. Avoidance of loud sound or shaking is critical for accurate evaluation.

Although the small movement M1 and the large movement M2 were also correlated with BMS at first, they gradually decreased during the follow-up period, as previously reported [9]. This might be due to the animal's habituation to the device, followed by lack of motivation. On the other hand, speed and acceleration did not decrease, suggesting that even a lackadaisical mouse had a moment to perform to its best ability during 5 min of observation. We also reconfirmed that the RG scores were almost zero in the contusion group, suggesting that it was difficult for C57BL/6 mice to stand up with only the hindlimbs after a 60-kdyn-contusive SCI.

Objectivity is one of the most important factors when evaluating motor function. While the open-field score is the simplest method, its value depends on the examiner, and subjectivity easily affects its accuracy [3]. Although evaluations using footprints or a treadmill seem objective, examiners discriminate certain parts or a range from the huge amount of data, so they still remain subjective [4, 5, 13]. In the present method, the values never vary by examiner and are calculated from the complete data, so they are always completely objective.

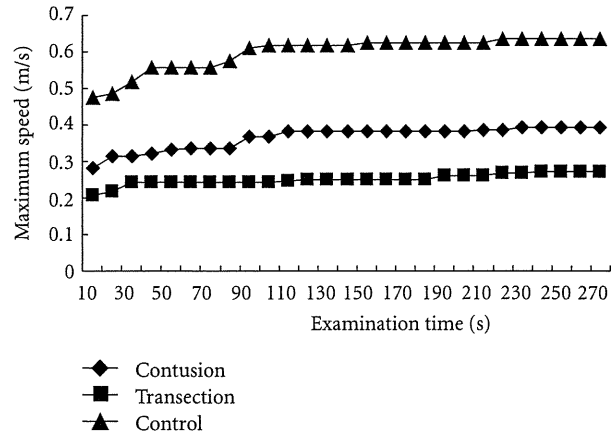

FIGURE 5: The maximum speed values to each time point were plotted with POD 42 data. They gradually increased and reached plateaus around 2 min in all groups. More than 2 minutes of examination time yielded slight difference.

Furthermore, ethical approval is necessary for animal studies, and the procedure must be as noninvasive as possible [14]. Behavioral analyses, such as the inclined test, beam walking test, and ladder test, cause mechanical stress to mice [7, 8, 15]. In belt-using devices, like a treadmill and automatic gait-recording machines, mouse behavior

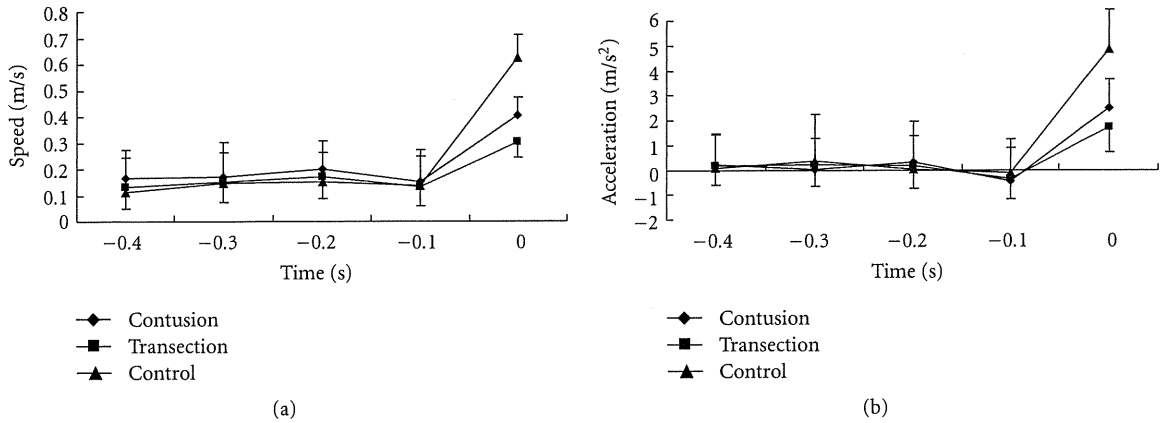

FIGURE 6: Shifting of the speed and acceleration just before reaching the maximum speed. Time 0 was the moment of maximum speed. Speed did not gradually increase to the maximum, and mice of all groups showed explosive power in 0.1 s to the maximum speed. Interestingly, acceleration 0.1 s before the maximum speed was under zero and that suggests muscles that were released just before strong contraction.

is severely restricted, and the moving belt sometimes harms the hindlimbs. With the present method, mice move freely as in a cage, and there is no stimulation and little stress. Hence, the present method is entirely noninvasive.

A simple and easy procedure is also desired for long-term follow-up of mice. Behavioral analysis, such as the inclined test, the beam walking test, or the ladder test, requires simple devices, but the cooperation of capricious mice is required, and examiners often have difficulty obtaining stable data. In contrast, using the present method, a mouse simply needs to be placed in the SCANET box, so that the acquisition of data is extremely easy.

5. Conclusion

In the evaluation of locomotor function in SCI model mice, inspections from various perspectives are desirable. Evaluation of maximum speed and acceleration of mouse movement with a SCANET system is simple, objective, and ethical. It is a novel and fine method for spinal cord-injured model mice and can complement other existing tests. Further examinations will be required for other animals.

Acknowledgments

The authors are grateful to Ms. Harada for the special care of the mice and to Drs. Nori and Yasuda for their excellent technical assistance during the surgical operations and data collection. This work was supported by the Project for Realization of Regenerative Medicine and Support for the core institutes for iPS cell research from the Ministry of Education, Culture, Sports, Science and Technology of Japan (MEXT).

References

[1] D. M. Basso, M. S. Beattie, and J. C. Bresnahan, "A sensitive and reliable locomotor rating scale for open field testing in rats," *Journal of Neurotrauma*, vol. 12, no. 1, pp. 1–21, 1995.

[2] D. M. Basso, L. C. Fisher, A. J. Anderson, L. B. Jakeman, D. M. McTigue, and P. G. Popovich, "Basso mouse scale for locomotion detects differences in recovery after spinal cord injury in five common mouse strains," *Journal of Neurotrauma*, vol. 23, no. 5, pp. 635–659, 2006.

[3] J. E. Beare, J. R. Morehouse, W. H. Devries et al., "Gait analysis in normal and spinal contused mice using the treadscan system," *Journal of Neurotrauma*, vol. 26, no. 11, pp. 2045–2056, 2009.

[4] M. Bervar, "Video analysis of standing—an alternative footprint analysis to assess functional loss following injury to the rat sciatic nerve," *Journal of Neuroscience Methods*, vol. 102, no. 2, pp. 109–116, 2000.

[5] L. de Medinaceli, W. J. Freed, and R. J. Wyatt, "An index of the functional condition of rat sciatic nerve based on measurements made from walking tracks," *Experimental Neurology*, vol. 77, no. 3, pp. 634–643, 1982.

[6] M. G. Fehlings, C. H. Tator, R. D. Linden, and I. R. Piper, "Motor and somatosensory evoked potentials recorded from the rat," *Electroencephalography and Clinical Neurophysiology*, vol. 69, no. 1, pp. 65–78, 1988.

[7] L. B. Goldstein and J. N. Davis, "Beam-walking in rats: studies towards developing an animal model of functional recovery after brain injury," *Journal of Neuroscience Methods*, vol. 31, no. 2, pp. 101–107, 1990.

[8] J. S. Soblosky, L. L. Colgin, D. Chorney-Lane, J. F. Davidson, and M. E. Carey, "Ladder beam and camera video recording system for evaluating forelimb and hindlimb deficits after sensorimotor cortex injury in rats," *Journal of Neuroscience Methods*, vol. 78, no. 1-2, pp. 75–83, 1997.

[9] Y. Mikami, M. Toda, M. Watanabe, M. Nakamura, Y. Toyama, and Y. Kawakami, "A simple and reliable behavioral analysis of locomotor function after spinal cord injury in mice: technical note," *Journal of Neurosurgery*, vol. 97, no. 1, pp. 142–147, 2002.

[10] W. B. J. Cafferty, N. J. Gardiner, P. Das, J. Qiu, S. B. McMahon, and S. W. N. Thompson, "Conditioning injury-induced spinal axon regeneration fails in interleukin-6 knock-out mice," *Journal of Neuroscience*, vol. 24, no. 18, pp. 4432–4443, 2004.

[11] Y. Mikami, H. Okano, M. Sakaguchi et al., "Implantation of dendritic cells in injured adult spinal cord results in activation of endogenous neural stem/progenitor cells leading to de novo

neurogenesis and functional recovery," *Journal of Neuroscience Research*, vol. 76, no. 4, pp. 453–465, 2004.

[12] K. Kawahats and M. Miyashita, "Electromyogram premotion silent period and tension development in human muscle," *Experimental Neurology*, vol. 82, no. 2, pp. 287–302, 1983.

[13] S. Rossignol, "Neural control of stereotypic limb movements," in *Handbook of Physiology*, L. B. Rowell and J. T. Sheperd, Eds., pp. 173–216, Oxford University Press, New York, NY, USA, 1996.

[14] H. Gee, "Animal guidelines," *Nature*, vol. 334, no. 6177, p. 7, 1988.

[15] A. S. Rivlin and C. H. Tator, "Objective clinical assessment of motor function after experimental spinal cord injury in the rat," *Journal of Neurosurgery*, vol. 47, no. 4, pp. 577–581, 1977.

OPEN ACCESS Freely available online

PLoS one

Visualization of Painful Experiences Believed to Trigger the Activation of Affective and Emotional Brain Regions in Subjects with Low Back Pain

Kazuhiro Shimo[1], Takefumi Ueno[2], Jarred Younger[3], Makoto Nishihara[1], Shinsuke Inoue[1], Tatsunori Ikemoto[4], Shinichirou Taniguchi[5], Takahiro Ushida[1,5]*

1 Multidisciplinary Pain Center, Aichi Medical University, Aichi, Japan, **2** Department of Neuropsychiatry, Kyushu University, Fukuoka, Japan, **3** Department of Anesthesia, School of Medicine, Stanford University, Stanford, California, United States of America, **4** NPO Pain Medicine Research Information Center, Kochi, Japan, **5** Department of Orthopaedic Surgery, Kochi Medical School, Kochi, Japan

Abstract

In the management of clinical low back pain (LBP), actual damage to lower back areas such as muscles, intervertebral discs etc. are normally targeted for therapy. However, LBP may involve not only sensory pain, but also underlying affective pain which may also play an important role overall in painful events. Therefore we hypothesized that visualization of a painful event may trigger painful memories, thus provoking the affective dimension of pain. The present study investigated neural correlates of affect processing in subjects with LBP (n = 11) and subjects without LBP (n = 11) through the use of virtual LBP stimuli. Whole brain functional magnetic resonance imaging (MRI) was performed for all subjects while they were shown a picture of a man carrying luggage in a half-crouching position. All subjects with LBP reported experiencing discomfort and 7 LBP subjects reported experiencing pain. In contrast to subjects without LBP, subjects with LBP displayed activation of the cortical area related to pain and emotions: the insula, supplementary motor area, premotor area, thalamus, pulvinar, posterior cingulate cortex, hippocampus, fusiform, gyrus, and cerebellum. These results suggest that the virtual LBP stimuli caused memory retrieval of unpleasant experiences and therefore may be associated with prolonged chronic LBP conditions.

Citation: Shimo K, Ueno T, Younger J, Nishihara M, Inoue S, et al. (2011) Visualization of Painful Experiences Believed to Trigger the Activation of Affective and Emotional Brain Regions in Subjects with Low Back Pain. PLoS ONE 6(11): e26681. doi:10.1371/journal.pone.0026681

Editor: Kazutaka Ikeda, Tokyo Metropolitan Institute of Medical Science, Japan

Received July 1, 2011; **Accepted** October 2, 2011; **Published** November 2, 2011

Funding: This work was supported by a Grant-in-Aid for Scientific Research from the Ministry of Health, Labour, and Welfare. The funders had no role in study design, data collection and analysis, decision to publish, or preparation of the manuscript.

Competing Interests: The authors have declared that no competing interests exist.

* E-mail: ushidat-koc@umin.ac.jp

Introduction

Psychological factors are known to affect the subjective experience of pain. Pain catastrophizing is one such maladaptive response to pain that is characterized by heightened pain intensity [1], increased disability [2]and difficulty disengaging from pain [3]. Recently, functional neuroimaging techniques have been developed that allow the neural correlates of psychological states to be explored. The blood oxygenation level-dependent contrast (BOLD-fMRI) is currently the most popular tool for mapping human brain activity [4]. Pain-related brain activations which could be considered as psychological factors have been reported in various studies. In healthy volunteers, several brain regions, including the primary and secondary somatosensory cortices, insula, anterior cingulate cortex (ACC), thalamus, and motor cortex, respond to real noxious stimuli and are regarded as part of the "pain matrix" [5,6]. However, it is also known that the expectation of pain can evoke brain activation patterns resembling that of a real pain experience [7].

In a previous study [8,9], Ogino reported that the imagination of pain even without physical injury engages the cortical representations of the pain-related neural network. Also, we reported that prior pain experiences can strongly affect pain anticipation and associated brain activations. We have also found that the anticipation of painful stimuli can cause the activation of cortical areas underlying pain-related affect in chronic neuropathic pain patients [10]. Activation in the brain during the visualization of a painful experience was found in the ACC and the medial prefrontalcortex (MPFC), which are regions known to be areas associated with pain and affect processing. Similar activations were found to be correlated with pain catastrophizing in individuals with fibromyalgia [11]. In that study, pain catastrophizing was associated with greater activity in the dorsolateral prefrontal cortex, rostral ACC, and MPFC, regions implicated in pain vigilance, attention and awareness [12,13,14,15]. These results suggest that pain-related neuronal activities might reflect the development and maintenance of chronic pain syndromes.

Low back pain (LBP) is one of the most common chronic pain syndromes. A recent fMRI study in humans reported actual LBP-related cerebral substrates [16]. Abnormal activations were identified in the prefrontal cortex, insula, thalamus, posterior cingulate cortex (PCC), supplementary motor area (SMA), and premotor areas (PMA) – predominantly in the right hemisphere.

Table 1. Evaluations of task-related discomfort and pain.

	LBP group (n = 11)	non-LBP group(n = 11)
Experiences evoked by tasks		
Discomfort (range)	3.5 (1–6)	0
Pain (range)	2.1 (0–6)	0
RDQ (mean ± SD)	3.1±3.1	0
ODI (mean ± SD)	19.8±7.8%	0

RDQ, Roland-Morris Disability Questionnaire; ODI, Oswestry Disability Index 2.0.
doi:10.1371/journal.pone.0026681.t001

We hypothesized that visualization of a painful experience would provoke unpleasant emotions, and these emotions might have a role in the maintenance of chronic pain syndromes. The present study investigated neural correlates of affect processing in subjects with nonspecific LBP and subjects without LBP by using virtual visual stimuli.

Results

Self-reported discomfort and pain (Table 1)

All subjects in the LBP group reported discomfort associated with viewing the simulated back pain (mean NRS score, 3.5; range, 1–6). 7 of the 11 subjects in the LBP group described pain associated with the task. However, no subjects in the non-LBP group reported any discomfort or pain resulting from viewing the picture of back pain.

fMRI results

Compared with the non-LBP group, the LBP group demonstrated significantly more activation in the left fusiform, as well as left inferior temporal gyrus, bilateral precentral gyrus, left middle frontal gyrus, left superior frontal gyrus, bilateral thalamus, bilateral caudate, right insula, left postcentral gyrus, bilateral lingual gyrus, bilateral parahippocampal gyrus, right superior temporal gyrus, left angular gyrus, left superior occipital gyrus, left precuneus, left middle temporal gyrus, left posterior cingulate cortex (PCC), and left cerebellum (Table 2,

Table 2. Talairach coordinates and Broadmann's areas for regions of statistically significant activation ($p<0.0005$ at voxel level uncorrected threshold) in response to virtual LBP stimulation (task – control condition).

Anatomical region	Side	Coordinate	Broadmann area	Z score
LBP group as compared to non-LBP group				
Fusiform gyrus	Lt	−46, −34, −13	Area 20	4.53
Inferior temporal gyrus	Lt	−57, −43, −15	Area 37	3.60
Precentral gyrus	Lt	−32, 8, 38	Area 9	4.38
	Rt	28, −24, 56	Area 4	4.03
Middle frontal gyrus	Lt	−46, 20, 43	Area 8	3.68
		−32, 11, 60	Area 6	3.50
Superior frontal gyrus	Lt	−40, 16, 53	Area 8	3.56
Thalamus	Lt	−24, −25, 7	-	4.34
	Rt	24, −27, 0	-	3.40
Caudate	Lt	−28, −32, 13	-	3.57
	Rt	38, −35, −3	-	3.91
Insula	Rt	28, −27, 12	Area 13	4.30
	Rt	34, −20, 18	Area 13	3.50
Postcentral gyrus	Lt	−8, −55, 64	Area 7	4.07
Lingual gyrus	Rt	18, −62, 0	Area 19	3.99
	Lt	−6, −72, −5	Area 18	3.81
Parahippocampal gyrus	Lt	−36, −43, 0	Area 19	3.96
	Rt	32, −53, −4	Area 19	3.91
	Rt	28, −41, −10	Area 36	3.62
Superior temporal gyrus	Rt	40, −35, 4	Area 41	3.78
Angular gyrus	Lt	−32, −74, 30	Area 39	3.88
Superior occipital gyrus	Lt	−38, −80, 33	Area 19	3.78
Precuneus	Lt	−42, −72, 35	Area 19	3.42
Middle temporal gyrus	Lt	−60, −35, −5	Area 21	3.62
Posterior cingulate gyrus	Lt	−10, −41, 30	Area 31	3.61
	Lt	−4, −43, 37	Area 31	3.55
Cerebellum	Lt	−24, −30, −20	-	3.88
non-LBP group as compared to LBP group				
Caudate	Rt	22, −34, 20	-	3.61

doi:10.1371/journal.pone.0026681.t002

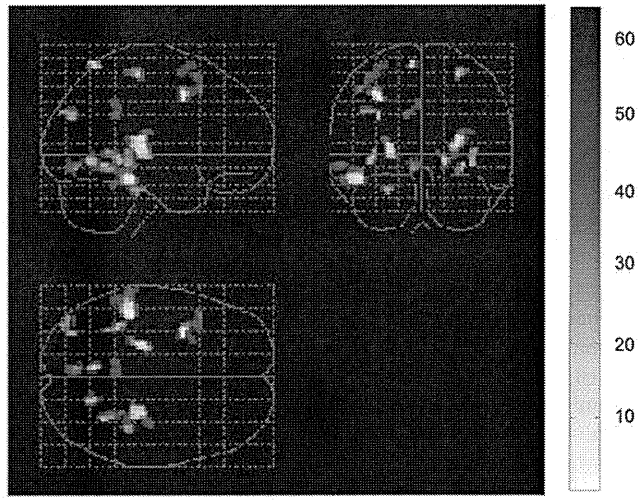

Figure 1. Areas of cortical activation in the LBP group compared with the non-LBP group in response to virtual LBP stimuli (task – control condition) detected by fMRI($p<0.0005$, Z score>3.4, uncorrected threshold).
doi:10.1371/journal.pone.0026681.g001

Fig. 1). The reverse contrast showed that the LBP group had lower activations than the non-LBP group in a single cluster in right caudate (Table 2).

In the LBP group, activations related to discomfort were found in the bilateral thalamus, bilateral medial frontal gyrus, right claustrum, left cerebellum (Table 3, Fig. 2). Activations associated with self-reported pain were found in the right thalamus and right lingual gyrus. RDQ scores were associated with activation in the left ACC, and ODI scores were associated with activations in the right insula (Table 3, Fig. 3).

Table 3. Cortial areas showing a linear signal increase with the discomfort rating, pain rating, RDQ scores and ODI scores.

Anatomical region	Side	Coordinate	Broadmann area	Z score
Discomfort				
Thalamus	Rt	20, −23, 5	-	4.19
	Lt	−4, −17, 3	-	3.78
Medial frontal gyrus	Rt	10, −22, 58	Area 6	3.85
	Lt	−12, −28, 53	Area 6	3.70
	Lt	−50, 1, 28	Area 6	3.38
Claustrum	Rt	30, 3, 13	-	3.75
Cerebellum	Lt	0, −53, −6	-	3.57
Pain				
Thalamus	Rt	20, −31, 7	-	4.27
Lingual gyrus	Rt	8, −86, −11	Area 18	3.62
RDQ				
Anterior cingulate gyrus	Lt	−6, 9, 27	Area 24	3.99
ODI				
Insula	Rt	40, −8, −5	Area 13	3.67

RDQ, Roland-Morris Disability Questionaire; ODI, Oswestry Disability Index 2.0.
doi:10.1371/journal.pone.0026681.t003

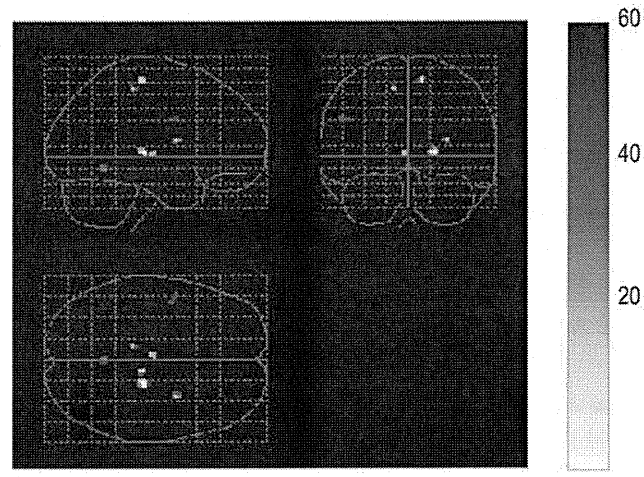

Figure 2. Areas of cortical activation showing an association with perceived discomfort.
doi:10.1371/journal.pone.0026681.g002

Discussion

Our results demonstrate that viewing images of simulated back pain evoke unpleasant feelings, and specific brain activations in individuals with LBP. According to the International Association for the Study of Pain, pain is defined as, "an unpleasant sensory and emotional experience associated with actual or potential tissue damage, or described in terms of such damage". As this definition suggests, both real pain stimuli and virtual pain experiences such as the visual stimuli in our study may play an important role in pain recognition and interpretation in the brain.

Functional MRI results showed that many of the areas described as being part of the "pain matrix" are also active during virtual pain. These results suggest that previous experiences of low back pain can sensitize an individual to pain anticipation. Activation in the insular cortex is associated with pain discrimination [17,18,19]. Additionally, the posterior insular cortex also plays a role in directing appropriate motor behaviors [20]. Furthermore, the insular cortex has projections to the SMA [21,22]. The SMA and PMA are commonly activated by pain [19,23], and usually associated with motor preparation. Activation in those areas might be associated with preparation for protective behavior against pain. In addition, we found virtual LBP stimuli led to increased activation in cerebellum. Activity in the cerebellum is frequently found in pain neuroimaging studies. Cerebellar activation is considered to be primarily associated with motor responses [13]. The need for temporally precise information may also be relevant for brain areas involved in initiating, propagating, and executing defensive motor responses to noxious stimuli [11,13,24,25].

The thalamus and the pulvinar are heavily interconnected with the visual and parietal cortices. Neuroimaging studies suggest responses in the pulvinar have a spatiotopic organization that are modulated by visual attention [26,27,28]. These results suggest that low back pain experiences may make individuals pay more attention to pain-related visual stimuli.

Many reports identify a role of the PCC in negative emotion [29,30,31,32,33,34], visuospatial orientation, and assessment of self-relevant sensation [35]. Exaggerated cerebral activation by pain stimuli may also be associated with pathologic pain states such as allodynia [36,37]. Together with its possible role in inflammatory pain [38], PCC activation could possibly reflect the negative emotion and the pathologic state of pain.

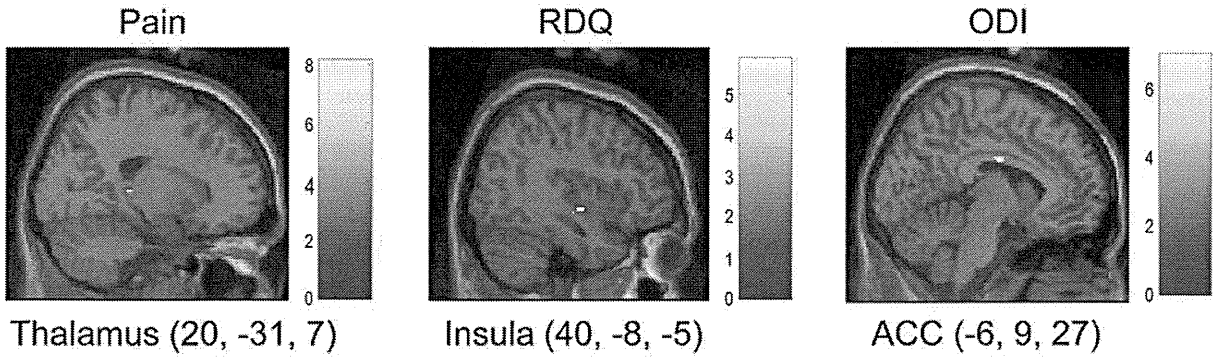

Figure 3. Sagittal sections showing cortical clusters where activity was linearly correlated with perceived pain, RDQ scores and ODI scores.
doi:10.1371/journal.pone.0026681.g003

We found other regions with heightened activity in LBP participants, in areas outside of the classic pain matrix. Those regions included the hippocampus, fusiform gyrus and angular gyrus. While not typically considered a nociceptive processing region, activation in the hippocampus has been previously reported to be activated in response to painful heat [14,39] and laser stimulation [40]. The hippocampus has been traditionally associated with recent memory consolidation [41], spatial memory [42], and fear-initiated avoidance behavior [43]. The hippocampus might also play a role in memorizing the pain stimulation and preparing fear-initiated avoidance. The fusiform gyrus is often associated with facial recognition [44]. It is conceivable, therefore, that our visual stimuli (which included a human face) may have been responsible for observed activations in the fusiform gyrus. However, our visual stimuli included a human facewithout any faical expression. This might suggest that the fusiform gyrus plays another important role in the cognitive neuroscience field. The angular gyrus is associated with empathy and 'theory of mind' [45]. Visual stimuli may cause subjects in the LBP group to imagine self pain or feel empathy towards the individual in pain in the picture.

Via parametric analyses in the LBP group, we identified several regional activations that were associated with discomfort rating, pain rating, RDQ scores and ODI scores. The SMA and PMA were related to the discomfort rating. As indicated previously, the SMA and PMA are involved in motor preparation. Activation in those areas might therefore be associated with preparation of protective behaviors against discomfort and pain. Thalamic activation was associated with both discomfort and pain ratings. Greater insula activation was associated with higher ODI scores. The thalamus and insula are considered part of the sensory component of pain processing [46]. But, a recent study suggests that imagining oneself in painful situations is sufficient to trigger some pain sensory regions [47]. The ACC was associated with RDQ scores. The ACC is an important part of affective pain processing [48,49] and can be activated in tasks of pain empathy [47,50,51,52,53,54,55]. It is unknown, therefore, whether the ACC activations, which were observed in the LBP group, were due to imagined self pain, or empathetic pain for the individual in the picture.

In this study, we showed that pain-related visual stimuli can activate several regions of the pain matrix in LBP patients, but not normal volunteers. Moreover, the pain questionnaire scores in the LBP patients were associated with greater activation of pain-processing brain regions. Functional MRI and the virtual visual tasks are non-invasive methods for probing pain-related fear and catastrophizing. These results might be applied to the evaluation of chronic pain syndromes, such as low back pain, in the future.

Materials and Methods

We recruited subjects with nonspecific LBP (LBP group) (n = 11, 6 male, 5 female, mean age 20.4 years) and subjects without LBP (non-LBP group) (n = 11, 5 male, 6 female, mean age 21.5 years). All participants were right-handed, had no history of cerebrovascular disease, and were free from any medication within 24 hours of the study. Scores for the Roland-Morris Disability Questionnaire (RDQ) and Oswestry Disability Index 2.0 (ODI) were obtained for all participants. Participants in the LBP group reported low back pain, and a RDQ or ODI score greater than zero. Participants in the non-LBP group had never experienced low back pain lasting longer than 1 week, and their RDQ and ODI scores were zero. No participants in either group displayed any evidence of structural abnormality in the lumbar spine on MRI, or any neurologic symptoms. None reported having a history of psychiatric disorders, or currently using any psychoactive medications.

We used virtual LBP stimuli depicting a man who is carrying luggage in a half-crouching position (Fig. 4). This picture represents an action that would likely cause pain in an individual with low back pain, and may therefore cause pain anticipation in the LBP group. Participants were also shown a picture depicting a man standing in front of luggage, providing the baseline stimulation (control condition) (Fig. 4). Participants in the LBP group had painful experiences in the half-crouching posture but did not have any pain in the standing posture. In addition, the participants in the LBP group currently feel little pain in daily life. During the fMRI session, trials were presented in a fixed block design. The distance between the participants' eyes and the screen was 12.5 cm, with a visual angle of $7.4 \times 11.3°$. The trials were applied eight times in each series, with each trial presentation lasting 3 seconds. The entire functional experiment lasted 150 seconds (see details of the experimental paradigm in Fig. 4). Self-reported discomfort and pain measures were collected using a numerical rating scale after the experimental session.

Images of the entire brain were acquired using GE SIGNA 3.0 Tesla scanner. Blood oxygenation level-dependent (BOLD) signals were collected with a T2-weighted, multi-slice, gradient echo-planar imaging (EPI) sequence (TE = 35 ms, TR = 3000 ms, flip angle = 90°, slice width = 4 mm, gap = 0 mm, 36 axial slices). Participants were scanned in the supine position, with the head

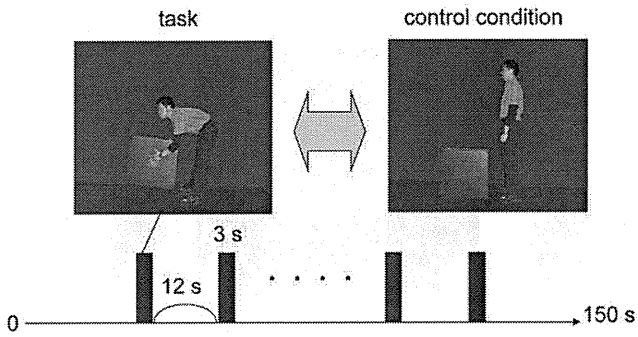

Figure 4. Experimental design. Subjects enrolled in the experiment were shown a picture demonstrating a man holding luggage in a half-crouching position (task picture) and a picture demonstrating a man standing in front of luggage, providing the baseline stimulation (control condition picture).
doi:10.1371/journal.pone.0026681.g004

fixed to minimize movement artifact. During the experiment, participants were simply instructed to observe the picture on screen.

The study was approved by the Ethical Committee of Kochi Medical School. All participants were informed of the study purpose beforehand and provided written consent to participate.

Results were analyzed on a Unix workstation using SPM2 (Statistical Parametric Mapping) software; Wellcome Department of Cognitive Neurology, Institute of Neurology, London: http://www.fil.ion.ucl.ac.uk/spm). The acquired images were realigned, spatially normalized to a standard EPI template and finally smoothed with an isotropic Gaussian kernel of 6 mm FWHM (full width at half maximum). Significance was assessed using the box car approach, convolved with the canonical hemodynamic response function. Activation maps represent t-test contrasts between the different experimental conditions. To identify the neural substrates for the virtual pain task, we contrasted the task condition and control condition in the LBP and non-LBP groups. Thresholds for activation were set at $p<0.0005$ for the voxel level of activation, and were further corrected for multiple comparisons at the cluster extent threshold of $p<0.05$. The Talairach atlas was used to anatomically localize foci of significant activation [56]. Brain activation between the LBP group and the non-LBP group was statistically compared to identify the neural processing specific to the LBP group ($p<0.05$, corrected, one-way ANOVA).

For the LBP group only, parametric analyses were also performed to determine associations between brain activity and perceived discomfort, perceived pain, RDQ score and ODI score. Normalized ratings were introduced at the subject level, taking into account only trials from the LBP group.

Acknowledgments

We would like to thank Mr. Kazuo Morio and Mr. Shin Yaogawa for technical assistance. We are grateful to KMS-TT group for the contributions of general research assistance.

Author Contributions

Conceived and designed the experiments: KS T. Ushida. Performed the experiments: KS T. Ushida. Analyzed the data: KS T. Ueno JY MN SI T. Ushida. Contributed reagents/materials/analysis tools: TI ST. Wrote the paper: KS T. Ueno JY T. Ushida.

References

1. Sullivan MJ, Rodgers WM, Kirsch I (2001) Catastrophizing, depression and expectancies for pain and emotional distress. Pain 91: 147–154.
2. Sullivan MJ, Lynch ME, Clark AJ (2005) Dimensions of catastrophic thinking associated with pain experience and disability in patients with neuropathic pain conditions. Pain 113: 310–315.
3. Van Damme S, Crombez G, Eccleston C (2004) Disengagement from pain: the role of catastrophic thinking about pain. Pain 107: 70–76.
4. Apkarian AV, Darbar A, Krauss BR, Gelnar PA, Szeverenyi NM (1999) Differentiating cortical areas related to pain perception from stimulus identification: temporal analysis of fMRI activity. J Neurophysiol 81: 2956–2963.
5. Qiu Y, Noguchi Y, Honda M, Nakata H, Tamura Y, et al. (2006) Brain processing of the signals ascending through unmyelinated C fibers in humans: an event-related functional magnetic resonance imaging study. Cereb Cortex 16: 1289–1295.
6. Wager TD, Rilling JK, Smith EE, Sokolik A, Casey KL, et al. (2004) Placebo-induced changes in FMRI in the anticipation and experience of pain. Science 303: 1162–1167.
7. Koyama T, McHaffie JG, Laurienti PJ, Coghill RC (2005) The subjective experience of pain: where expectations become reality. Proc Natl Acad Sci U S A 102: 12950–12955.
8. Ogino Y, Nemoto H, Inui K, Saito S, Kakigi R, et al. (2007) Inner experience of pain: imagination of pain while viewing images showing painful events forms subjective pain representation in human brain. Cereb Cortex 17: 1139–1146.
9. Ushida T, Ikemoto T, Tanaka S, Shinozaki J, Taniguchi S, et al. (2008) Virtual needle pain stimuli activates cortical representation of emotions in normal volunteers. Neurosci Lett 439: 7–12.
10. Ushida T, Ikemoto T, Taniguchi S, Ishida K, Murata Y, et al. (2005) Virtual pain stimulation of allodynia patients activates cortical representation of pain and emotions: a functional MRI study. Brain Topogr 18: 27–35.
11. Gracely RH, Geisser ME, Giesecke T, Grant MA, Petzke F, et al. (2004) Pain catastrophizing and neural responses to pain among persons with fibromyalgia. Brain 127: 835–843.
12. Bornhovd K, Quante M, Glauche V, Bromm B, Weiller C, et al. (2002) Painful stimuli evoke different stimulus-response functions in the amygdala, prefrontal, insula and somatosensory cortex: a single-trial fMRI study. Brain 125: 1326–1336.
13. Buchel C, Bornhovd K, Quante M, Glauche V, Bromm B, et al. (2002) Dissociable neural responses related to pain intensity, stimulus intensity, and stimulus awareness within the anterior cingulate cortex: a parametric single-trial laser functional magnetic resonance imaging study. J Neurosci 22: 970–976.
14. Derbyshire SW, Jones AK, Gyulai F, Clark S, Townsend D, et al. (1997) Pain processing during three levels of noxious stimulation produces differential patterns of central activity. Pain 73: 431–445.
15. Valet M, Sprenger T, Boecker H, Willoch F, Rummeny E, et al. (2004) Distraction modulates connectivity of the cingulo-frontal cortex and the midbrain during pain–an fMRI analysis. Pain 109: 399–408.
16. Kobayashi Y, Kurata J, Sekiguchi M, Kokubun M, Akaishizawa T, et al. (2009) Augmented cerebral activation by lumbar mechanical stimulus in chronic low back pain patients: an FMRI study. Spine (Phila Pa 1976) 34: 2431–2436.
17. Henderson LA, Gandevia SC, Macefield VG (2007) Somatotopic organization of the processing of muscle and cutaneous pain in the left and right insula cortex: a single-trial fMRI study. Pain 128: 20–30.
18. Korotkov A, Ljubisavljevic M, Thunberg J, Kataeva G, Roudas M, et al. (2002) Changes in human regional cerebral blood flow following hypertonic saline induced experimental muscle pain: a positron emission tomography study. Neurosci Lett 335: 119–123.
19. Svensson P, Minoshima S, Beydoun A, Morrow TJ, Casey KL (1997) Cerebral processing of acute skin and muscle pain in humans. J Neurophysiol 78: 450–460.
20. Berthier M, Starkstein S, Leiguarda R (1988) Asymbolia for pain: a sensory-limbic disconnection syndrome. Ann Neurol 24: 41–49.
21. Augustine JR (1996) Circuitry and functional aspects of the insular lobe in primates including humans. Brain Res Brain Res Rev 22: 229–244.
22. Luppino G, Matelli M, Camarda R, Rizzolatti G (1993) Corticocortical connections of area F3 (SMA-proper) and area F6 (pre-SMA) in the macaque monkey. J Comp Neurol 338: 114–140.
23. Hsieh JC, Stahle-Backdahl M, Hagermark O, Stone-Elander S, Rosenquist G, et al. (1996) Traumatic nociceptive pain activates the hypothalamus and the periaqueductal gray: a positron emission tomography study. Pain 64: 303–314.
24. Peyron R, Kupers R, Jehl JL, Garcia-Larrea L, Convers P, et al. (2007) Central representation of the RIII flexion reflex associated with overt motor reaction: an fMRI study. Neurophysiol Clin 37: 249–259.
25. Sullivan MJ, Thorn B, Haythornthwaite JA, Keefe F, Martin M, et al. (2001) Theoretical perspectives on the relation between catastrophizing and pain. Clin J Pain 17: 52–64.
26. Cotton PL, Smith AT (2007) Contralateral visual hemifield representations in the human pulvinar nucleus. J Neurophysiol 98: 1600–1609.

27. Fischer J, Whitney D (2009) Precise discrimination of object position in the human pulvinar. Hum Brain Mapp 30: 101–111.
28. Smith AT, Cotton PL, Bruno A, Moutsiana C (2009) Dissociating vision and visual attention in the human pulvinar. J Neurophysiol 101: 917–925.
29. Benuzzi F, Lui F, Duzzi D, Nichelli PF, Porro CA (2008) Does it look painful or disgusting? Ask your parietal and cingulate cortex. J Neurosci 28: 923–931.
30. Britton JC, Phan KL, Taylor SF, Welsh RC, Berridge KC, et al. (2006) Neural correlates of social and nonsocial emotions: An fMRI study. Neuroimage 31: 397–409.
31. Maddock RJ, Garrett AS, Buonocore MH (2003) Posterior cingulate cortex activation by emotional words: fMRI evidence from a valence decision task. Hum Brain Mapp 18: 30–41.
32. Mantani T, Okamoto Y, Shirao N, Okada G, Yamawaki S (2005) Reduced activation of posterior cingulate cortex during imagery in subjects with high degrees of alexithymia: a functional magnetic resonance imaging study. Biol Psychiatry 57: 982–990.
33. Sander K, Frome Y, Scheich H (2007) FMRI activations of amygdala, cingulate cortex, and auditory cortex by infant laughing and crying. Hum Brain Mapp 28: 1007–1022.
34. Sinha R, Lacadie C, Skudlarski P, Wexler BE (2004) Neural circuits underlying emotional distress in humans. Ann N Y Acad Sci 1032: 254–257.
35. Vogt BA (2005) Pain and emotion interactions in subregions of the cingulate gyrus. Nat Rev Neurosci 6: 533–544.
36. Freund W, Wunderlich AP, Stuber G, Mayer F, Steffen P, et al. (2010) Different activation of opercular and posterior cingulate cortex (PCC) in patients with complex regional pain syndrome (CRPS I) compared with healthy controls during perception of electrically induced pain: a functional MRI study. Clin J Pain 26: 339–347.
37. Lorenz J, Cross DJ, Minoshima S, Morrow TJ, Paulson PE, et al. (2002) A unique representation of heat allodynia in the human brain. Neuron 35: 383–393.
38. Ruehle BS, Handwerker HO, Lennerz JK, Ringler R, Forster C (2006) Brain activation during input from mechanoinsensitive versus polymodal C-nociceptors. J Neurosci 26: 5492–5499.
39. Ploghaus A, Narain C, Beckmann CF, Clare S, Bantick S, et al. (2001) Exacerbation of pain by anxiety is associated with activity in a hippocampal network. J Neurosci 21: 9896–9903.
40. Bingel U, Quante M, Knab R, Bromm B, Weiller C, et al. (2002) Subcortical structures involved in pain processing: evidence from single-trial fMRI. Pain 99: 313–321.
41. Alvarez P, Squire LR (1994) Memory consolidation and the medial temporal lobe: a simple network model. Proc Natl Acad Sci U S A 91: 7041–7045.
42. Clark RE, Broadbent NJ, Squire LR (2007) The hippocampus and spatial memory: findings with a novel modification of the water maze. J Neurosci 27: 6647–6654.
43. Hollup SA, Kjelstrup KG, Hoff J, Moser MB, Moser EI (2001) Impaired recognition of the goal location during spatial navigation in rats with hippocampal lesions. J Neurosci 21: 4505–4513.
44. Radua J, Phillips ML, Russell T, Lawrence N, Marshall N, et al. (2010) Neural response to specific components of fearful faces in healthy and schizophrenic adults. Neuroimage 49: 939–946.
45. Vollm BA, Taylor AN, Richardson P, Corcoran R, Stirling J, et al. (2006) Neuronal correlates of theory of mind and empathy: a functional magnetic resonance imaging study in a nonverbal task. Neuroimage 29: 90–98.
46. Bushnell MC, Duncan GH, Hofbauer RK, Ha B, Chen JI, et al. (1999) Pain perception: is there a role for primary somatosensory cortex? Proc Natl Acad Sci U S A 96: 7705–7709.
47. Jackson PL, Brunet E, Meltzoff AN, Decety J (2006) Empathy examined through the neural mechanisms involved in imagining how I feel versus how you feel pain. Neuropsychologia 44: 752–761.
48. Apkarian AV, Bushnell MC, Treede RD, Zubieta JK (2005) Human brain mechanisms of pain perception and regulation in health and disease. Eur J Pain 9: 463–484.
49. Davis KD, Taylor KS, Hutchison WD, Dostrovsky JO, McAndrews MP, et al. (2005) Human anterior cingulate cortex neurons encode cognitive and emotional demands. J Neurosci 25: 8402–8406.
50. Botvinick M, Jha AP, Bylsma LM, Fabian SA, Solomon PE, et al. (2005) Viewing facial expressions of pain engages cortical areas involved in the direct experience of pain. Neuroimage 25: 312–319.
51. Gu X, Han S (2007) Attention and reality constraints on the neural processes of empathy for pain. Neuroimage 36: 256–267.
52. Jackson PL, Meltzoff AN, Decety J (2005) How do we perceive the pain of others? A window into the neural processes involved in empathy. Neuroimage 24: 771–779.
53. Lamm C, Batson CD, Decety J (2007) The neural substrate of human empathy: effects of perspective-taking and cognitive appraisal. J Cogn Neurosci 19: 42–58.
54. Morrison I, Lloyd D, di Pellegrino G, Roberts N (2004) Vicarious responses to pain in anterior cingulate cortex: is empathy a multisensory issue? Cogn Affect Behav Neurosci 4: 270–278.
55. Singer T, Seymour B, O'Doherty J, Kaube H, Dolan RJ, et al. (2004) Empathy for pain involves the affective but not sensory components of pain. Science 303: 1157–1162.
56. Talairach J, Tournoux P (1988) Co-planar Stereotaxic Atlas of the Human Brain. New York: Thime Medical Publishers. 122 p.

Spine

SPINE Volume 36, Number 10, pp 778–783

BIOMECHANICS

In Vivo Three-Dimensional Kinematics of the Cervical Spine During Head Rotation in Patients With Cervical Spondylosis

Yukitaka Nagamoto, MD,* Takahiro Ishii, MD, PhD,† Hironobu Sakaura, MD, PhD,‡ Motoki Iwasaki, MD, PhD,‡ Hisao Moritomo, MD, PhD,‡ Masafumi Kashii, MD, PhD,§ Takako Hattori, MD,* Hideki Yoshikawa, MD, PhD,‡ and Kazuomi Sugamoto, MD, PhD*

Study Design. Kinematics of the cervical spine during head rotation was investigated using 3-dimensional (3D) magnetic resonance imaging (MRI) in patients with cervical spondylosis (CS).

Objective. To demonstrate *in vivo* 3D kinematics of the spondylotic cervical spine during head rotation.

Summary of Background Data. Several *in vivo* studies have identified kinematic differences between normal and spondylotic subjects, but only two-dimensional flexion/extension motion has been investigated. Differences of *in vivo* 3D cervical motion during head rotation between normal and spondylotic subjects have yet to be clarified.

Methods. Ten healthy volunteers (control group) and 15 patients with CS (CS group) underwent 3D MRI of the cervical spine with the head rotated to 5 positions (neutral, ±45° and ±maximal head rotation). Relative motions of the cervical spine were calculated by automatically superimposing a segmented 3D MRI of the vertebra in the neutral position over images for each position using volume registration. The 3D motions of adjacent vertebra were represented with 6 degrees of freedom by Euler angles and translations on the coordinate system.

Results. Compared with the control group, the CS group showed significantly decreased mean axial rotation and mean coupled lateral bending at C5–C6 and C6–C7 and significantly increased mean coupled lateral bending at C2–C3 and C3–C4, although both the groups showed the same pattern of coupled motions.

Conclusion. The *in vivo* 3D kinematics of the spondylotic cervical spine during head rotation was accurately depicted and compared with those of healthy cervical spines for the first time.

Key words: kinematics, coupled motion, cervical spondylosis, volume registration. **Spine 2011;36:778–783**

The human cervical spine is composed of highly specific tissues and structures, which together provide the extensive range of motion and considerable load-carrying capacity required for physical activities of daily living (ADL). This is 1 reason why degenerative changes in the cervical spine start as early as middle age and affect more than 95% of patients older than 65 years.[1] Even though nerve root or cord compression develops in 10% to 15% of the population,[2] the pathophysiology of cervical spondylosis (CS) remains poorly understood.[3]

Achieving a better understanding of this pathophysiology requires clarification of the differences in kinematics between the normal and spondylotic cervical spine. Several kinematic studies associated with aging and/or degeneration of the cervical spine have been reported using simple extension and flexion radiography,[4–7] motion analysis,[8] cineradiography,[9] and magnetic resonance imaging (MRI).[10] However, most of these studies have investigated only 2-dimensional flexion/extension motion, and 3-dimensional (3D) analysis using a motion analyzer has been vague and indirect. No study comparing in vivo 3D cervical motion during head rotation between normal and spondylotic subjects has been conducted, despite the importance of these motions in ADL. This is because of the difficulty in measuring *in vivo* cervical segmental motion, particularly during head rotation and lateral bending, which involves complex 3D motions called "coupled motion." We have developed a 3D MRI system to evaluate the *in vivo* 3D kinematics of the spine[11–14] and have already reported accurate *in vivo* 3D kinematics of the normal cervical spine using this method.[11–13] The objectives of this study were to investigate *in vivo* 3D kinematics of the spondylotic cervical spine during head rotation and to compare those with kinematics of the healthy cervical spine.

From the *Department of Orthopaedic Biomaterial Science Osaka University Graduate School of Medicine; †Department of Orthopaedic Surgery, Kaizuka City Hospital, Kaizuka; ‡Department of Orthopaedics, Osaka University Graduate School of Medicine; and §Department of Orthopaedic Surgery, Toyonaka Municipal Hospital, Shibahara, Toyonaka, Osaka, Japan.

Acknowledgment date: October 28, 2009. Revision date: March 13, 2009. Acceptance date: March 18, 2010.

The manuscript submitted does not contain information about medical device(s)/drug(s).

No funds were received in support of this work. No benefits in any form have been or will be received from a commercial party related directly or indirectly to the subject of this manuscript.

This study was approved by IRB of our institute.

Address correspondence and reprint requests to Yukitaka Nagamoto, MD, Department of Orthopaedic Biomaterial Science, Osaka University Graduate School of Medicine, 2-2 Yamadaoka, Suita, Osaka 5650871, Japan; E-mail: 7gam0to@gmail.com

DOI: 10.1097/BRS.0b013e3181e218cb

MATERIALS AND METHODS

Subjects in this study comprised 10 healthy volunteers (control group) and 15 patients with CS (CS group). The 10 healthy volunteers (5 men, 5 women; mean age, 25.1 years; range, 22–31 years) had neither neck pain nor any medical history of cervical spine disorders. As for the control group, all subjects were included in our previous publications[11–13] and retrospective analysis was performed. The 15 patients (7 men, 8 women; mean age, 60.2 years; range, 41–70 years) had been referred to our institution because of axial and/or neurologic symptoms and showed radiographic findings of CS as follows: loss of disc space height; spondylotic bars; foraminal osteophytes; and kyphosis. Subjects with a history of cervical spine surgery, trauma, tumors, infection, rheumatoid arthritis, or ossification of the posterior longitudinal ligament were excluded. All study protocols were approved in advance by the institutional review board.

Each subject was placed supine on the MRI table and underwent 3D MRI in 5 positions with the head rotated 0° (neutral position), 45°, and maximally to the left and right. All subjects were instructed to rotate the head as perpendicular as possible to the axis of the body trunk, and the shoulders were fixed to the table with a band. In the control group, MRI was performed using a 1.0-T commercial magnetic resonance system (Signa LX; General Electric, Milwaukee, WI). A 3D fast-gradient recalled acquisition in the steady state sequence was used with the following settings: repetition time, 8.0 ms; echo time, 3.3 ms; slice thickness, 1.5 mm; no interslice gap; flip angle, 10°; field of view, 24 cm; and 256 × 224 in-plane acquisition matrix. In the CS group, MRI was performed using a 1.5-T commercial magnetic resonance system (MAGNETOM Espree; Siemens, Erlangen, German). A 3D multiecho data imaging combination sequence was used with the following settings: repetition time, 40.0 ms; echo time, 20.0 ms; slice thickness, 1.3 mm; no interslice gap; flip angle, 12°; field of view, 24 cm; and 256 × 226 in-plane acquisition matrix. All subjects provided informed consent to undergo 3D MRI for the kinematics study and those for whom MRI proved difficult to perform because of axial and/or neurologic symptoms were excluded. All examinations were performed by the first or second author.

MRI data were saved in Digital Imaging and Communications in Medicine format and transmitted to a computer workstation, where image processing was performed using software developed in our laboratory (Virtual Place M series; Medical Imaging Laboratory, Tokyo, Japan). The method used in this study has been fully described in previous reports[11–13] and is, therefore, only described briefly here. This method showed high accuracy as follows: 0.24° for flexion/extension, 0.31° for lateral bending, 0.43° for axial rotation, 0.52 mm for superoinferior translation, 0.51 mm for anteroposterior translation, and 0.41 mm for lateral translation.[11] As a result of image processing (volume registration method), 3D motions of each vertebra expressed as a matrix were obtained. For easier comprehension of complicated 3D motions, relative 3D cervical motions of all motion segments were calculated by converting the matrix obtained by image processing into a matrix representing relative motion with respect to the inferior adjacent vertebra, and these motions were expressed in 6 degrees of freedom by Euler angles with the sequence of yaw (X)-pitch (Y)-roll (Z) and translations using a previously defined coordinate system as follows: the z-axis of occipital bone (Oc) was parallel to the line connecting anterior and posterior borders of the foramen magnum, with anterior considered positive. The y-axis was defined as perpendicular to the z-axis, with superior being positive. The x-axis was positive to the left. The coordinate system of C1 was defined using 2 points: the posteroinferior border of the anterior arch and the anteroinferior border of the posterior arch. Origins were located at the anterior border of the foramen magnum on Oc and the posteroinferior border of the anterior arch on C1. The coordinate system of subaxial cervical vertebrae was defined as follows: the origin was located at the most inferior point on the posterior wall of the vertebral body in the midsagittal plane. The z-axis was defined as the line connecting anterior and posterior points in the inferior plane of the vertebral body, with anterior considered positive. The y-axis was defined as perpendicular to the z-axis, with superior being positive. The positive x-axis was directed to the left (Figure 1).[11–13] The coordinate system was always set with moving vertebrae (suprajacent vertebra of the functional spinal unit) in this study. Mean values and standard

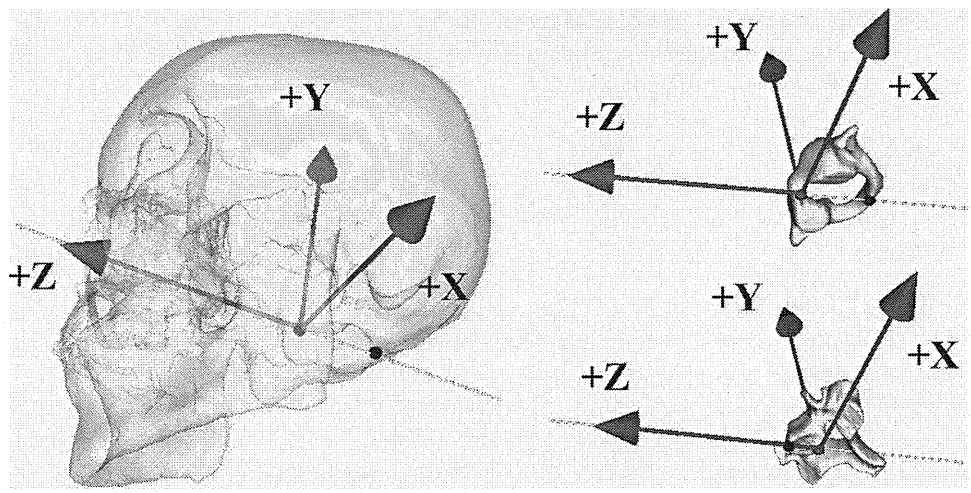

Figure 1. Anatomic orthogonal coordinate system for Oc, C1, and subaxial cervical vertebrae (C5). The methods have been fully described in previous studies.